UNIVERSITY OF LEEDS

This is a repository copy of *Continuous flow synthesis of MOF UTSA-16(Zn), mixed-metal and magnetic composites for CO_2 capture – toward scalable manufacture*.

White Rose Research Online URL for this paper:
https://eprints.whiterose.ac.uk/id/eprint/224618/

Version: Accepted Version

Article:

Woodliffe, J.L., Molinar-Díaz, J., Clowes, R. et al. (5 more authors) (2024) Continuous flow synthesis of MOF UTSA-16(Zn), mixed-metal and magnetic composites for CO_2 capture – toward scalable manufacture. Journal of Environmental Chemical Engineering, 12 (6). 114167. ISSN 2213-2929

https://doi.org/10.1016/j.jece.2024.114167

This is an author produced version of an article published in the Journal of Environmental Chemical Engineering, made available under the terms of the Creative Commons Attribution License (CC-BY), which permits unrestricted use, distribution and reproduction in any medium, provided the original work is properly cited.

Reuse

This article is distributed under the terms of the Creative Commons Attribution (CC BY) licence. This licence allows you to distribute, remix, tweak, and build upon the work, even commercially, as long as you credit the authors for the original work. More information and the full terms of the licence here: https://creativecommons.org/licenses/

Takedown

If you consider content in White Rose Research Online to be in breach of UK law, please notify us by emailing eprints@whiterose.ac.uk including the URL of the record and the reason for the withdrawal request.

White Rose
university consortium
Universities of Leeds, Sheffield & York

eprints@whiterose.ac.uk
https://eprints.whiterose.ac.uk/

Continuous flow synthesis of MOF UTSA-16(Zn), mixed-metal and magnetic composites for CO_2 capture – toward scalable manufacture

John Luke Woodliffe[a], *Jesús Molinar-Díaz*[b], *Rob Clowes*[c], *Oday H Hussein*[d], *Ed Lester*[a], *Rebecca Ferrari*[e], *Ifty Ahmed*[a], *Andrea Laybourn*[a*]

a) Advanced Materials Research Group, Faculty of Engineering, University of Nottingham, Nottingham, NG7 2RD, UK
b) Composites Research Group, Faculty of Engineering, University of Nottingham, Nottingham, NG7 2RD, UK
c) Department of Chemistry and Materials Innovation Factory, University of Liverpool, L69 3BX, UK
d) Department of Materials Science and Engineering, University of Sheffield, S1 4ND, UK
e) Food Water Waste Research Group, Faculty of Engineering, University of Nottingham, Nottingham, NG7 2RD, UK

*Corresponding author. Email: andrea.laybourn@nottingham.ac.uk

Keywords: metal-organic framework, magnetic framework composite, magnetic nanoparticles, induction heating, carbon capture, adsorption.

Abstract

UTSA-16(Zn) is a zinc and citrate-based metal-organic framework (MOF) which has shown highly promising performance for CO_2 capture. However, the transition of this MOF to industrial application has been hindered as a scalable synthesis method has not yet been reported. Herein we report the first scalable continuous flow synthesis of UTSA-16(Zn), demonstrating a production rate of 173 g/h, which is a 77-fold increase compared to previously reported batch methods. Sustainability of the synthesis was maximised using low-cost non-toxic reagents and a low-energy flow reactor operating at atmospheric pressure. Chemical (reactant ratios, Zn/Mg mixed-metal) and process parameters (solvent ratio, flow rate, temperature) were optimised to continuously produce UTSA-16(Zn) which also demonstrated a high CO_2 adsorption capacity up to 3.8 mmol/g and conversion yield of up to 66%. Pristine MOFs are typically thermally insulating, thus thermal regeneration is challenging. To overcome this limitation, magnetic nanoparticles can be embedded within the MOF. This enables fast and energy efficient regeneration through magnetic induction heating. Here, citrate-coated Fe_3O_4 magnetic nanoparticles (MNP-CA) were successfully incorporated into the flow synthesis process of UTSA-16(Zn) to form UTSA-16(Zn)@MNP-CA magnetic framework composites (MFCs), representing the highest production rate reported of any MFC to date (152 g/h c.f. 13 g/h for $MgFe_2O_4$@UiO-66-NH_2). UTSA-16(Zn)@MNP-CA MFCs demonstrate rapid heating under a magnetic field (26-150 °C in 60 s). The flow method developed herein is also widely applicable for scalable manufacture of other MOFs and MFCs, enabling their broader transition towards industrial applications.

Graphical abstract

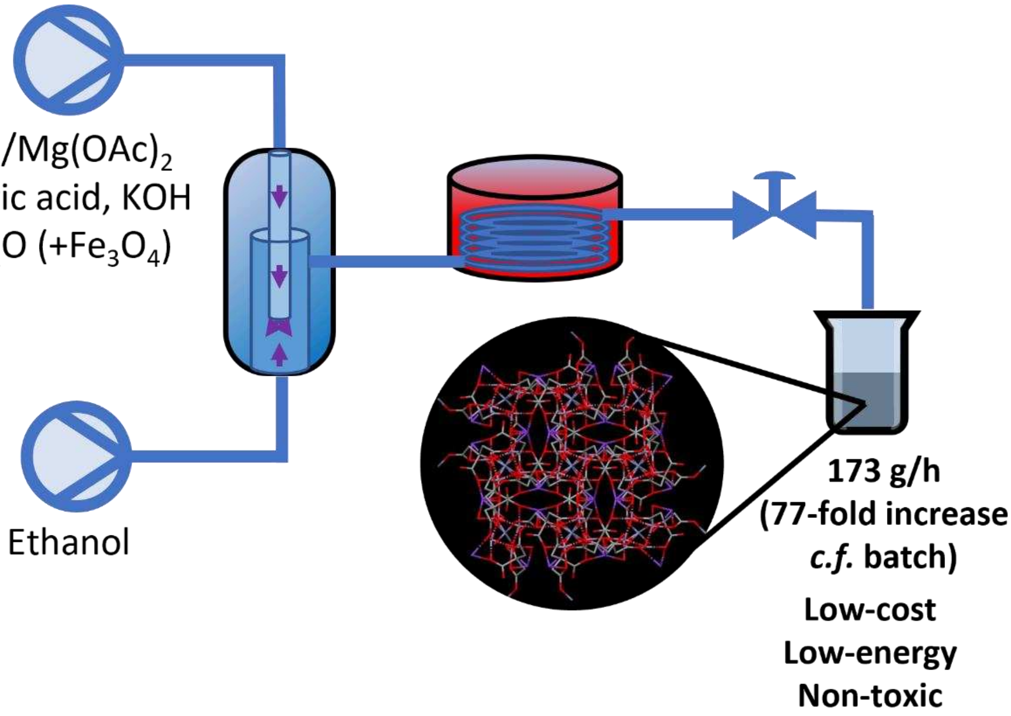

1 Introduction

Achieving net-zero greenhouse gas emissions is a key priority for governments and industries worldwide to minimise the on-going devastating impacts of climate change. To reach these targets, CO_2 capture will play a vital role[1]. CO_2 can be captured at its largest sources, power plants, through post-combustion capture facilities, which can be retrofitted into existing plants[2]. Currently amine technologies are used, however, these suffer from solvent decomposition/degradation and have very high energy requirements (e.g. 3.5-8 MJ/kg CO_2 for monoethanolamine)[3–5], limiting widescale deployment and use[6].

Porous solid adsorbents are considered an energy-efficient alternative for CO_2 capture[7], with significantly reduced energy for CO_2 separation and material regeneration for reuse[8]. Metal-organic frameworks (MOFs) are a class of porous materials containing metal ions/clusters and organic linkers[9]. They are of particular interest in CO_2 capture applications due to their tailorable structures with high capacities and selectivities for CO_2[10]. MOF UTSA-16 (UTSA: University of Texas at San Antonio) has been identified as a current top-performing material in a recent review considering a range of metrics across different porous materials for carbon capture (alongside zeolite 13X and IISERP-MOF2)[7]. In particular, UTSA-16(Zn) ($C_{12}H_8KO_{14}Zn_3$, a zinc and citrate-based MOF) has shown strong potential for industrial-scale CO_2 capture applications due to its high CO_2 adsorption capacity (1.7 mmol/g) and selectivity CO_2/N_2 (>100) at the partial pressures relevant for post-combustion capture (0.15 bar)[11]. Importantly, UTSA-16(Zn) also shows good stability to moisture and acid gases (only a 6% and 10% decrease in capacity after exposure to 25 ppm NO_2 and SO_2, respectively)[12], and low production costs (<1 USD/g) due to the low-cost and abundant starting reagents[12].

To translate MOFs from the lab to commercial settings, the ability to manufacture them at the required quality, scale, and cost is essential. As such, principles of sustainable development and the circular economy are also important, such as minimising energy, raw materials, reagent toxicity and waste, and designing materials for reuse and recyclability[13]. Moving from a batch to continuous production process is therefore highly beneficial, as it offers rapid manufacture (due to enhanced heat and mass transfer), improved reproducibility, lower solvent, and energy consumption, higher space-time yield (STY) and reactor scalability, alongside reduced downtime and labour costs (as there are fewer steps between batches)[14,15]. Owing to these advantages, extensive research has been undertaken on the development of continuous flow syntheses for several MOFs, especially for archetypal MOFs such as HKUST-1, MIL-53, UiO-66, and ZIF-8[16–18].

Despite the advancements in flow chemistry for MOF production[16,18,19], and the benefits of UTSA-16(Zn) for CO_2 capture applications, no scalable synthesis has yet been developed for this particular MOF. Herein we report the first continuous flow synthesis of MOF UTSA-16(Zn), with a very high production rate of 173 g/h and an STY of 23573 kg/m^3/day. These represent a 77-fold and 15-fold increase in the production rate and STY respectively, compared to the highest previously reported for the MOF[20]. This marks a significant step towards production at industrially relevant scales and subsequent application. In addition, we sought to maximise reaction sustainability, considering only low-cost, non-toxic, and non-anhydrous reagents/solvents and a low energy atmospheric pressure reactor, without the use of vacuum drying.

After synthesising the sorbent material and adsorbing CO_2, the next important step is separating CO_2 from the adsorbent to regenerate the material for reuse. However, the thermally insulating nature of MOFs makes thermal regeneration highly challenging, particularly at scale[21]. A promising approach to address this limitation is to incorporate magnetic nanoparticles (MNPs) in the MOF, forming materials known as magnetic framework composites (MFCs)[20,22–24]. The inclusion of magnetic nanoparticles in the MOF enables rapid and energy-efficient regeneration by localised magnetic induction heating[25]. This process is known as magnetic induction swing adsorption (MISA)[26] and has demonstrated remarkably low energy costs associated with CO_2 capture and release (1.29 MJ/kg of CO_2), 45% below commercially deployed materials[27]. Induction heating for regeneration has also been explored for zeolites[28], and has shown promise for biomass upgrading[29,30] and ethylene/ethane separation applications.[31] It is also possible to use magnetic composites in electric swing adsorption (ESA). ESA is similar to MISA in that an electric current provides the source of heating, however, ESA relies on resistive Joule heating, which is better suited to monoliths[32] rather than powders or pellets for CO_2 capture, as electricity must be passed through the adsorption column for the desorption step[33].

In this study, an in-depth optimisation of the flow synthesis for UTSA-16(Zn) is presented, evaluating the influence of chemical parameters such as reagent ratios and concentrations, alongside an investigation into mixed-metal syntheses using magnesium, which is reported to increase CO_2 adsorption capacity[34]. Physical process parameters were also investigated, including flow rate, solvent ratio, and temperature. Furthermore, citrate-coated Fe_3O_4 magnetic nanoparticles (MNP-CA) were incorporated into MOF UTSA-16(Zn) using our continuous flow method, resulting in the highest reported production rate of any MFC to-date (152 g/h), demonstrating a scalable and sustainable synthesis for the MFC UTSA-16(Zn)@MNP-CA with advantages for use in post-combustion CO_2 capture. The flow method developed herein is also applicable towards scalable manufacture of other MOFs and MFCs, aiding the broader transition of these exciting materials from the lab towards real-world applications.

2 Material and Methods

2.1 Materials

All reagents and chemicals were used as originally received and water was deionised. Zinc acetate dihydrate (≥99.0%), magnesium acetate tetrahydrate (≥99.0%), potassium hydroxide (86.7%) and citric acid monohydrate (≥99.0%) and were purchased from Sigma Aldrich. Methanol (≥99.9%) was bought from Fisher Scientific, ethanol (absolute, SpS grade) from Scientific Laboratory Supplies LTD and ammonium iron citrate (14.5-16% Fe basis) from Honeywell.

2.2 Synthesis of UTSA-16(Zn) and UTSA-16(Zn,Mg)

Synthesis of UTSA-16(Zn) was performed using a counter-current continuous flow reactor customized from perfluoroalkoxy (PFA) polymer tubing (O.D: 6 mm, I.D: 4 mm) (Figure 1). Zinc acetate dihydrate (3-5 mmol), magnesium acetate tetrahydrate (0-2 mmol), citric acid monohydrate (4-6 mmol) and potassium hydroxide (12-20 mmol) were dissolved in water (10 mL) and fed *via* the downflow pump into the top of the reactor (10-80 mL/min). Water was then fed *via* the downflow pump after the reaction solution. Ethanol absolute (anti-solvent) was fed *via* the upflow pump into the bottom of the reactor (10-80 mL/min) resulting in an overall ratio of H_2O:EtOH between 2:1 and 1:2. After mixing and precipitation, the reaction stream was heated through a 14 m PFA coil (OD: 6 mm, ID: 4 mm) in a water bath (25-85 °C, residence time: 1-9 min). A back-pressure regulator was used to prevent rapid boiling of the solvent mixtures for the reaction heated to 85 °C. The product (white solid) was then collected in suspension at the reactor outlet, centrifuged (5000 RPM) and washed with methanol (3 x 30 mL) before drying at 75 °C in an oven overnight (yield: 0.1-0.8 g, conversion yield: 9-66%, production rate: 21-341 g/h). Conversion yield was calculated as a percent of the obtained product mass over the theoretical maximum product mass from the reaction. All materials produced were consistent with the UTSA-16 structure by PXRD (without any remaining starting materials), except for the alternative crystalline phase discussed in section 3.1 (Supplementary Information, Figures S1-S9). Experimental conditions for each reaction can be found in the Supplementary Information, Tables S1-S8).

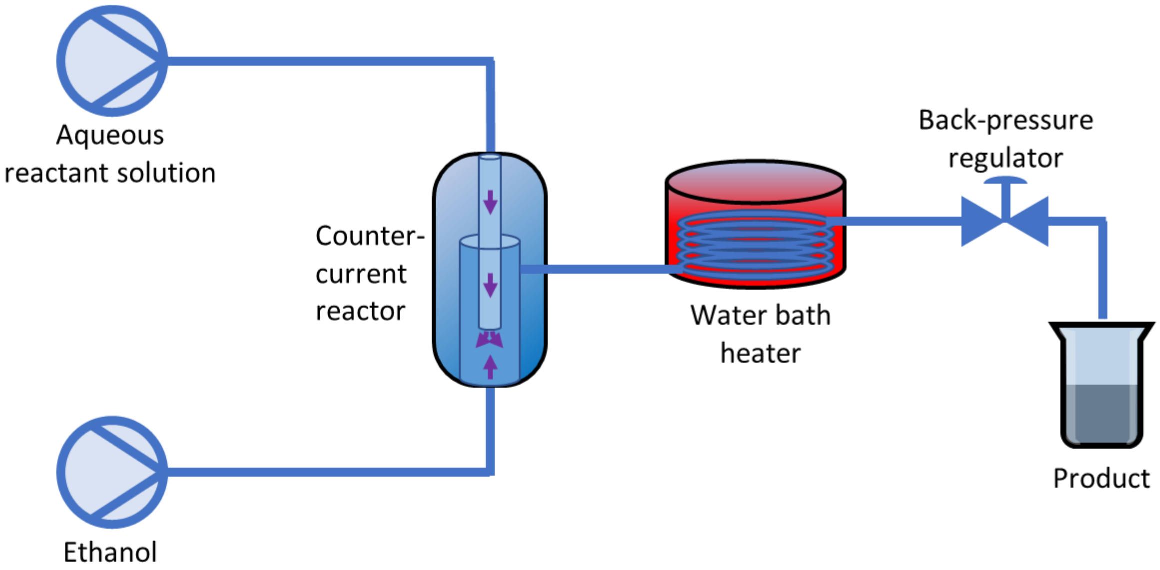

Figure 1: Schematic of the counter-current continuous flow reactor set-up used for the synthesis of UTSA-16(Zn), UTSA-16(Zn,Mg) and UTSA-16(Zn)@MNP-CA MFCs.

2.3 Extended reaction scale-up synthesis of UTSA-16(Zn)

The synthesis of UTSA-16(Zn) was scaled-up using the optimised procedure from section 2.2, with a larger volume of reagents (10-fold increase compared to previous optimisation reactions). Zinc acetate dihydrate (0.05 mol), citric acid monohydrate (0.05 mol) and potassium hydroxide (0.15 mol) were dissolved in water (100 mL) and fed *via* the downflow pump into the top of the reactor (40 mL/min). Ethanol absolute was fed *via* the upflow pump into the bottom of the reactor (40 mL/min). The water bath heating temperature was 80 °C. After collection at the reactor outlet, the product (white solid) was centrifuged (5000 RPM) and washed with methanol (3 x 300 mL) before drying at 75 °C in an oven overnight (yield: 7.2 g, conversion yield: 59%, production rate: 173 g/h). To investigate the impact of further solvent exchange, a portion of the product (0.8 g) was separated from the rest before drying and was subjected to additional washing and solvent exchange steps with methanol over 5 days (6 x 40 mL).

2.4 Synthesis of citrate-coated magnetic magnetite nanoparticles (MNP-CA)

Magnetic nanoparticles (citrate-coated magnetite, MNP-CA) were produced as previously reported using a counter-current continuous-flow hydrothermal reactor[20]. Briefly, an aqueous solution of ammonium ferric citrate (0.05 M) was fed into the bottom of the reactor at 10 mL/min. As a separate stream, deionised water was heated to 435 °C using a 2 kW band heater and fed into the top of the reactor at 20 mL/min. The pressure was kept at 24 MPa using a back-pressure regulator and cooled through a heat exchanger. The product MNP-CA was collected at the reactor outlet in suspension, separated through gravity and magnetic attraction, washed using deionised water (3 x 25 mL) and stored as a 5% w/v suspension.

2.5 Synthesis of UTSA-16(Zn)@MNP-CA magnetic framework composites (MFCs)

UTSA-16(Zn)@MNP-CA was synthesised based on the procedure outlined in section 2.2. Zinc acetate dihydrate (5 mmol), citric acid monohydrate (5 mmol) and potassium hydroxide (15 mmol) were first dissolved in water (8-9.5 mL). A 5% w/v solution of MNP-CA in water was then added (0.5-2 mL), bringing the total water quantity to 10 mL, and the solution fed *via* the downflow pump into the top of the reactor (40 mL/min). Water was then fed *via* the downflow pump after the reaction solution. Ethanol absolute was fed *via* the upflow pump into the bottom of the reactor (40 mL/min) resulting in an overall ratio of H_2O:EtOH of 1:1. After mixing and precipitation, the reaction stream was heated through the water bath coil (80 °C, residence time: 2 min). The product (brown solid) was then collected in suspension at the outlet, centrifuged (5000 RPM) and washed with methanol (3 x 30 mL) before drying at 75 °C in an oven overnight (yield: 0.63 g, conversion yield: 49-52%, production rate: 152 g/h).

2.6 Characterisation

Powder X-ray diffraction (PXRD). Patterns of UTSA-16(Zn), MNP-CA, and UTSA-16(Zn)@MNP-CA (2.9%, 11.4%) were acquired from a Bruker D8 Advance DaVinci with a Lynxeye 1D detector (Bragg-Brentano geometry). The radiation source was Cu K_α (λ = 0.15406 nm, 40 KV, 40 mA). Scans ranged from 5° to 45° 2θ and Bruker DIFFRAC.EVA software was used for pattern matching with files from the database[35].

Scanning electron microscopy (SEM). Secondary electron images were obtained from a Jeol 7000F FEG-SEM (Jeol PC-SEM software), with 10-15 kV acceleration voltage, 10 mm working distance and 10 nm carbon coating.

Mineral liberation analysis/energy dispersive X-ray spectroscopy (MLA/EDS). For chemical and mineral distribution analyses, specimens were first embedded in a cold epoxy resin and sectioned by mechanical grinding using 1200 SiC grit papers and polishing using 6 µm and 1 µm diamond paste. The polished samples were then cleaned using industrial methylated spirit (IMS) and dried before carbon coating. Backscattered electron (BSE) imaging and chemical analyses of the samples were performed using scanning electron microscopy (SEM, FEI Quanta600 MLA; 20 kV; spot size 7) based mineral liberation analysis (MLA), equipped with energy dispersive X-ray spectroscopy (EDS) for compositional analysis and linked Bruker/JKTech/FEI data acquisition software for automated mineralogy.

Thermogravimetric analysis (TGA). A TA instruments TGA550 Discovery was used for TGA analyses. Thermal decomposition was measured under an air atmosphere at a 10 °C/min heating rate. CO_2 adsorption capacity was measured gravimetrically[36] using the following program: ramp to 150 °C (N_2), isothermal 10 min, ramp to 25 °C, switch gas (CO_2), isothermal 10 min. CO_2 adsorption-desorption cycling used a similar program, with an initial 150 °C activation, then a 60 °C regeneration for each desorption step. CO_2 adsorption was performed at 25 °C.

N_2 and CO_2 adsorption isotherms. N_2 isotherms were obtained from a Micromeritics ASAP 2020 V4.04 instrument at 77 K, and surface area was determined through the Brunauer-Emmett-Teller (BET) method. CO_2 adsorption isotherms were measured at 273 K and 298 K using the same instrument. Heats of adsorption were calculated using the Clausius–Clapeyron approach from the CO_2 adsorption isotherms.

Vibrating-sample magnetometry (VSM). Magnetisation was measured at room temperature up to 10 kOe with a Quantum Design SQUID MPMS3.

Induction heating. Samples were heated using a Cheltenham Induction Heating Ltd induction heater with a water-cooled copper coil (2 kW, 204 kHz), according to a previously reported procedure[24]. Briefly, 0.5 g sample powder was heated in a borosilicate glass tube (500 W), with the temperature measured by a Neoptix Reflex fibre optic thermocouple.

Inductively coupled plasma optical emission spectroscopy (ICP-OES). ICP-OES measurements were taken using an Agilent 5110 Vertical Dual View instrument with 240 place SPS-4 autosampler. Instrument operation and data processing was via the Agilent 'ICP Expert' software package. UTSA-16(Zn,Mg) samples were digested in nitric acid (5% aqueous) prior to atomization in an argon plasma (5000-8000 K). Results were taken in triplicate.

3 Results and Discussion

UTSA-16(Zn), UTSA-16(Zn,Mg) and UTSA-16(Zn)@MNP-CA were synthesised using a customised pipe-in-pipe counter-current continuous flow reactor, chosen due to its simple design and rapid mixing capabilities, as described in the experimental section (Figure 1). The reactor was based on a design first reported by Lester *et al.* in 2006 to produce various nanoparticles[37], which has since also been used in the manufacture of archetypal MOFs such as HKUST-1, ZIF-8, and CPO-27/MOF-74[38,39]. The customised reactor used in this study was made from transparent perfluoroalkoxy polymer tubing due to its high chemical resistance, also facilitating high flow rates and visual observations during synthesis. The flow after mixing is laminar, with calculated Reynolds numbers of approximately 80-322 for the 40-160 mL/min flow rates.

An initial scoping study was used to identify variables with the greatest influence on yield and CO_2 adsorption capacity and to obtain standard values (values chosen for each variable while another variable was changed).

Table 1 displays each variable tested, the standard values and the ranges optimised in the study. These variables were then systematically varied one-at-a-time to optimise synthesis conditions and examine the influence of each on yield (%, based on the theoretical conversion) and CO_2 adsorption (measured gravimetrically using TGA[36]).

Table 1: Variables investigated for the synthesis optimisation study, alongside their minimum, maximum and standard values (values chosen for each variable while another variable was changed).

Variable	**Min value**	**Max value**	**Standard value**	**Comments**
Citric acid concentration (M)	0.4	0.6	0.5	Linker:base ratio kept at 1:3
KOH concentration (M)	1.30	1.95	1.5	
Mg metal mole fraction in reactants [Mg]/[Mg+Zn]	0.0	0.4	0.0	Total metal concentration [Mg+Zn] kept at 0.5 M
Solvent ratio $[H_2O]/[H_2O+EtOH]$	0.33	0.67	0.50	
Total flow rate (mL/min)	40	160	80	
Water bath temperature (°C)	25	90	80	At T>80 °C a back-pressure regulator was used to prevent boil-off
MNP-CA concentration in product (wt%)	0.0	11.4	0.0	Quantified using saturation magnetisation measurements

3.1 Optimisation of chemical parameters to maximise yield and CO_2 adsorption capacity

Initial work concentrated on the optimisation of chemical parameters to maximise the yield and CO_2 adsorption capacity of UTSA-16(Zn). The metal concentration was fixed at 0.5 M and citric acid concentration was varied from 0.4 to 0.6 M, keeping a linker:base (L:B) ratio of 1:3. Results (Figure 2A) show that CO_2 adsorption capacity increased from 2.1 to 3.8 mmol/g as linker concentration increased from 0.4 to 0.6 M. The yield stayed around 50% up to a linker concentration of 0.5 M after which the yield decreased from 50 to 25%. These yield values are similar to other MOF flow syntheses, such as 59% for MIL-53(Al)[40], 27% for HKUST-1[19] and 24-78% for UiO-66[41]. The ratio of Zn:L:B in UTSA-16(Zn) calculated from the empirical formula ($C_{12}H_8KO_{14}Zn_3$)[11] is 3:2:1. The Zn:L:B ratio used in the literature synthesis is typically 1:1:3[11,12,34], meaning that linker and base are in excess. The metal to linker ratio in MOF synthesis is typically known to have a significant effect on MOF structure and topology[42]. For instance, Zhou *et al.* showed that Zn-based MOFs PCN-13, PCN-131 and PCN-132 could each be produced by altering the metal to linker (anthrancene-9,10-dicarboxylic acid) reactant molar ratio between 1:1 and 5:1[43]. The crystallinity of MOF-5 and CO_2 adsorption of Cu-BTC (BTC = 1,3,5-benzenetricarboxylate) also depend on the metal to linker ratio[44,45]. In this study, PXRD patterns of reaction products revealed that the higher linker to metal ratios resulted in a higher degree of crystallinity in the case of UTSA-16(Zn). The relative degree of crystallinity was compared between samples by considering the reciprocals of the full width half maximum (1/FWHM)[46,19] of the main 7.4 °2θ peak in the PXRD pattern of the MOFs. In this study, crystallinity increased from 3.0 to 5.0 as linker concentration increased from 0.4 to 0.6 M (Figure S2, Supplementary Information). This increase in degree of crystallinity (decrease in FWHM) corresponds with the CO_2 adsorption capacity increase from 2.1 to 3.8 mmol/g. The correlation between degree of crystallinity and sorption capacity has also been observed experimentally with ZIF-8[47] and HKUST-1[48] in line with our results.

The linker concentration was then fixed at 0.5 M (balancing the optimal yield of 50% and high CO_2 adsorption capacity of 3.6 mmol/g), and the concentration of KOH (base) was varied from 1.30 to 1.95 M (Figure 2B). The yield peaked at 50% for a base concentration of 1.50 M before decreasing to 9% when the concentration of KOH increased from 1.50 to 1.95 M. CO_2 adsorption capacity remained high (3.3-3.6 mmol/g between 1.5 and 1.8 M KOH), with sharp decreases outside of that range to 1.4 mmol/g at 1.30 M KOH and 1.0 mmol/g at 1.95 M KOH. The effect of base concentration/pH is well documented in various MOF syntheses. It is typically considered that linker deprotonation occurs more rapidly at higher pH values, resulting in faster MOF nucleation, as with Zn-based MOF-5, HKUST-1 and Dy(BTC)(H_2O) MOF crystals, with an impact on sorption characteristics[49]. PXRD patterns obtained herein showed that the degree of crystallinity for UTSA-16(Zn) increased with base concentration, with crystallinity increasing from 5.2 to 5.7 from 1.3 to 1.73 M KOH (Figure S3, Supplementary Information). This increase in degree of crystallinity corresponded with an increase in CO_2 adsorption capacity from 1.4 to 3.5 mmol/g. Above 1.8 M KOH, an alternative unknown crystalline phase formed (different to the typical UTSA-16(Zn) tetragonal crystal system, space group: I-42d)[11], with new peaks at 9, 10 and 13 °2θ (Figure S3, Supplementary Information). This phase could be the result of very rapid linker deprotonation at higher pH (1.8 M KOH), resulting in the formation of an alternative framework structure. This result has also been observed for Co^{2+} with H_3BTC MOFs, where partial or full deprotonation at different pH values resulted in the formation of alternate framework structures with differing sorption characteristics[50]. A value of 1.5 M for the base concentration was then taken forward, giving both optimal yield (50%) and CO_2 adsorption capacity (3.6 mmol/g).

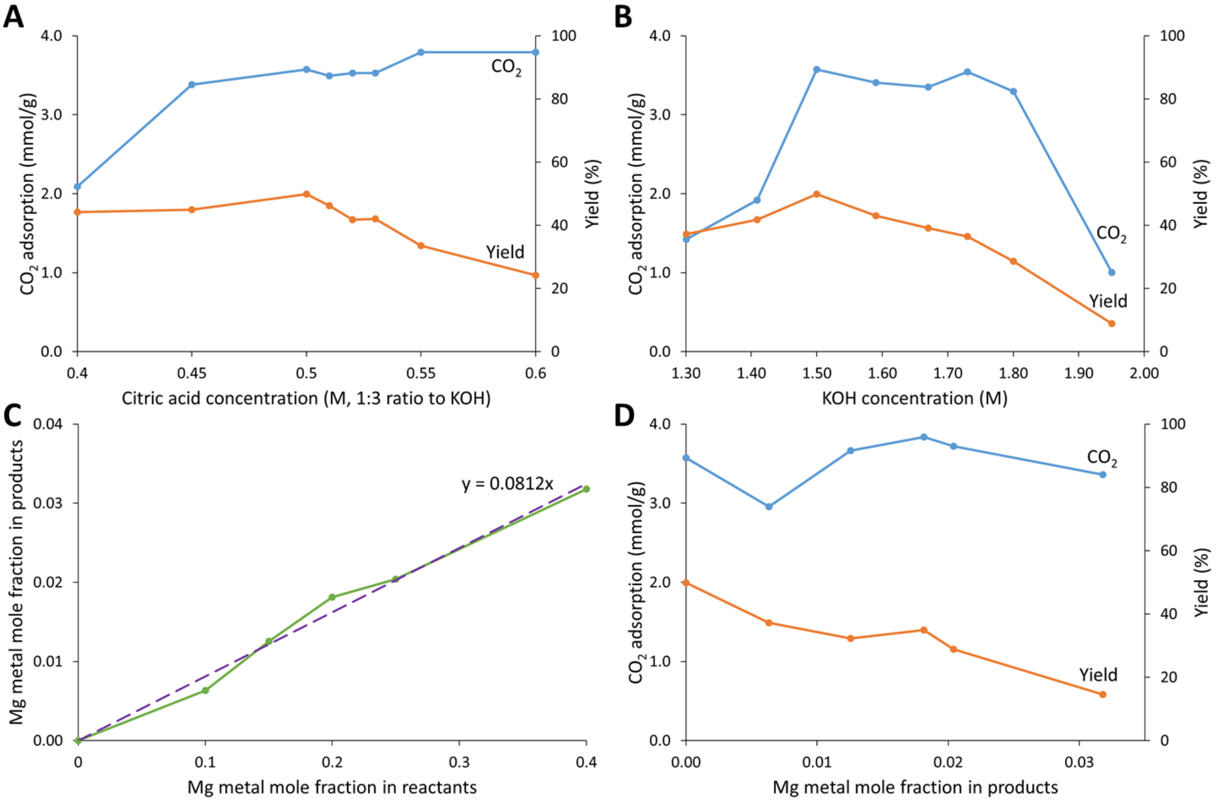

Figure 2: CO_2 adsorption capacity and yield of UTSA-16(Zn) plotted against A: citric acid concentration (a linker:base ratio of 1:3 was maintained) and B: KOH concentration. C: Mg metal mole fraction in the reactants plotted against observed Mg metal mole fraction in the products. D: CO_2 adsorption capacity and yield of UTSA-16(Zn,Mg) plotted against Mg metal mole fraction in the products by ICP-OES analysis.

Mixed-metal MOFs contain more than 1 type of metal ion/cluster within the frameworks and can be prepared by simply using a combination of metal salts during synthesis[51]. Often this one-pot synthesis strategy results in an approximately homogeneous dispersion of the metal ions in the MOF[52]. The combination of metals can be advantageous due to a tuning of the functionality of the MOF, including improvements to CO_2 adsorption capacity and CO_2/N_2 selectivity[53]. Recently Gaikwad *et al.* showed that various metals can be incorporated into UTSA-16 via a 4 h microwave heating method[34]. They found that synthesising UTSA-16 with a 7:2 ratio of Zn:Mg increased CO_2 capacity by 18% and CO_2/N_2 selectivity by 19%

(141 *cf.* 118) compared to pristine UTSA-16(Zn) in their method, attributed to an increase in surface area and open metal sites in the bimetallic MOF[34]. A study to incorporate Mg into UTSA-16(Zn) via our rapid flow synthesis method was therefore conducted. ICP-OES analysis showed that the actual concentrations of Mg incorporated in the UTSA-16(Zn,Mg) products were significantly less than those included in the reactants, approximately 8% of the expected values (*e.g.* 0.4 Mg metal mole fraction in reactants resulted in 0.032 Mg metal mole fraction in the final product) (Figure 2C). MOF formation seemed to favour Zn^{2+} over Mg^{2+} during the very short timescales of our synthesis (2 min residence time). Gaikwad *et al.* observed 84% incorporation of Mg^{2+} from the starting reagents into their UTSA-16(Zn,Mg) product, using a 7:2 weight ratio of Zn:Mg in their microwave batch method[54]. However, this was determined by SEM/EDS mapping, which is a more qualitative technique (complex topographies can introduce uncontrolled geometric factors, resulting in systematic errors, often by a factor of ten or more)[55]. Preferential incorporation of certain cations over others has also been observed in the literature for mixed-metal MOFs, and can be attributed to a number of factors including solubility, reactivity, and coordination sphere of the metal ions[56]. This effect is also observed for incorporation of Ni^{2+} into UTSA-16(Co), where only partial incorporation of Ni^{2+} was achieved[57].

Figure 2D shows the impact on CO_2 adsorption capacity and yield of the increasing Mg^{2+} metal mole fraction ([Mg]/[Mg+Zn]) in the mixed-metal products. The yield decreased from 50% to 15% with increasing Mg^{2+} metal mole fraction in the products from 0 to 0.032. The limited incorporation of Mg^{2+} was likely a contributor to the trend in decreasing yield with increasing Mg^{2+} mole fraction. CO_2 adsorption capacities of the materials peaked at 3.8 mmol/g at a Mg^{2+} mole fraction of 0.018, an increase of 0.2 mmol/g (6%) compared to pristine UTSA-16(Zn) without Mg^{2+}. The differences in CO_2 adsorption capacity after Mg^{2+} inclusion into UTSA-16(Zn,Mg) could have arisen from changes in pore sizes, as with other mixed-metal Zr/Ti MOFs[58], since Mg^{2+} has a slightly smaller ionic radius (0.066 nm) compared to Zn^{2+} (0.074 nm)[59]. Changes to the open metal sites of MOFs by introducing mixed-metals is frequently reported to impact CO_2 adsorption capacity (due to different strengths of interactions between CO_2 and the metal nodes), such as in MIL-101(Cr,Mg)[60] and the Mg-mixed CPM-200 series[53]. However, interactions with K^+ counterions in the pores are key to the CO_2 adsorption capacity of UTSA-16[61,62], so it is less likely that changes in open-metal sites are the cause of changing CO_2 capacity for this MOF. PXRD patterns showed an increase in the degree of crystallinity (from 4.5 to 5.7) going from no Mg^{2+} to a Mg^{2+} mole fraction of 0.018 (Figure S4, Supplementary Information) as CO_2 adsorption capacity increased from 3.6 to 3.8 mmol/g. Mg^{2+} therefore impacted crystallisation, and polyhedra size (measured by SEM image analysis (n=100)) increased from 62±19 nm to 92±28 nm diameter from no Mg^{2+} to a Mg^{2+} mole fraction of 0.018 in the bimetallic MOF (Figure S13, Supplementary Information). Finally, Mg^{2+} was found to be well-distributed throughout the MOF by mineral liberation analysis (MLA) with energy dispersive X-ray spectroscopy (EDS) (Figure S15, Supplementary Information).

3.2 Optimisation of process parameters to maximise yield and CO_2 adsorption capacity

Once chemical parameters had been optimised, focus then shifted to optimising the physical processing variables for the synthesis of UTSA-16(Zn). As described in the experimental section, our flow rig (Figure 1) included an aqueous reactant solution pump and an ethanol solvent pump. The ratio of these two pumps (ensuring the total flow rate was kept constant) was varied from 1:2 H_2O:EtOH (0.33 solvent fraction H_2O) to 2:1 H_2O:EtOH (0.67 solvent fraction H_2O). The associated impact on CO_2 adsorption capacity and yield are shown in Figure 3A. A ratio of 1:1 gave an optimal CO_2 adsorption capacity of 3.6 mmol/g, though yield could be increased from 50% to 55% by increasing the EtOH antisolvent ratio from H_2O:EtOH 1:1 to 1:1.3. This increase in EtOH ratio did, however, result in a lower CO_2 adsorption capacity of 3.4 mmol/g. PXRD patterns showed that at high H_2O ratios the degree of crystallinity for UTSA-16(Zn) reduced (from 4.5 to 3.4), going from H_2O:EtOH 1:1 to 2:1. This reduction corresponded with a decrease in CO_2 adsorption capacity from 3.6 to 1.8 mmol/g, as discussed previously in section 3.1. At a high EtOH ratio (H_2O:EtOH 1:2), low intensity peaks corresponding to an alternative crystal structure were observed in the PXRD pattern (Figure S5, Supplementary Information). These reflections are the same as those observed in the PXRD pattern at high pH (1.8 M KOH) described earlier in section 3.1 (Figure S3, Supplementary Information). This further supports our hypothesis that an alternative structure arises from faster nucleation than the usual UTSA-16(Zn) phase, as high EtOH antisolvent ratios result in very rapid nucleation. A similar rate of formation effect is reported for modulated synthesis of MOFs, where the addition of a modulator slows down the self-assembly process, changing the phase or topology of MOF produced[63]. An example is the use of benzoic acid as a modulator to influence the kinetics of the self-assembly of MIL-101(Cr), resulting in the formation of an alternative structure, MIL-88B(Cr)[64]. SEM images herein showed the formation of rod-like crystals in the 1:2 H_2O:EtOH sample containing the alternative PXRD structure, attributed to a new phase, which is not visible in the samples at other solvent ratios (Figure S13, Supplementary Information). In addition to influencing rate of formation, solvents are also known to play a significant role in the synthesis and morphology of MOFs [65,66]. An example is the various crystal structures of Mg PDC MOFs (PDC = pyridine dicarboxylate) produced by different solvents under the same reaction conditions[65]. Variation of H_2O:EtOH solvent ratio also affects the crystallisation process of Mg BTC MOFs[66], where the solvent ratios produced different structures due to the solubility properties and coordination behaviour of the metal cations.

Keeping the H_2O:EtOH solvent ratio at 1:1, the total flow rate was varied between 40 and 160 mL/min (Figure 3B). The yield of UTSA-16(Zn) product increased steeply from 29% to 50% as flow rate increased from 40 mL/min to 80 mL/min, before gradually decreasing to 45% as flow rate increased further to 160 mL/min. This trend likely represents a combination of two overlapping factors, dominant in different flow-rate ranges. These factors are mixing intensity in the counter-current reactor (see Figure 1) which increases with flow rate[67] and has dominant impact at flow rates <80 mL/min, and residence time in the laminar-flow water bath heater (see Figure 1) which decreases with increasing flow rate and dominates at flow rates >80 mL/min. Both factors are influenced by flow rate[68]. To investigate these factors further, an experiment was performed where the flow rate of the reaction mixture through the counter-current reactor was 160 mL/min, after which the flow rate was lowered to 20 mL/min as the reaction mixture passed through the water bath heater (maximising both initial mixing intensity in the counter-current reactor and residence time in the water bath heater). The data points from this experiment are marked with triangular symbols in Figure 3B. The UTSA-16(Zn) product yield was higher than that recovered for the synthesis performed at a flow rate of 160 mL/min through both the counter-current reactor and water bath heater (60% *cf.* 45%), showing that a longer residence time in the water bath heater produces a higher yield for a set counter-current reactor flow rate (160 mL/min).

CO_2 adsorption capacity increased from 3.0 to 3.6 mmol/g as flow rate increased from 40 mL/min to 80 mL/min, before gradually decreasing to 3.1 mmol/g as flow rate increased further to 160 mL/min. However, CO_2 adsorption capacity of the UTSA-16(Zn) synthesised with a 160 mL/min counter-current reactor flow rate and 20 mL/min water bath heater flow rate (triangular data point, Figure 3B) matched that measured for the product of the reaction kept at 160 mL/min throughout. This shows that longer residence time in the water bath heater was not beneficial for CO_2 adsorption capacity, and mixing intensity in the counter-current reactor is the dominant factor. It is therefore proposed that mass transfer/mixing efficiency is optimised around 80 mL/min for our rig, and greater flow rates/intensity don't result in more efficient mixing[69]. An optimal mixing intensity is therefore crucial for optimising the synthesis of UTSA-16(Zn) and must be carefully considered if transferring the synthesis to an alternative flow-rig or scaling up the reactor size[70].

PXRD patterns of UTSA-16(Zn) collected at different flow rates (40-160 mL/min) again showed the link between CO_2 adsorption capacity and degree of crystallinity, with degree of crystallinity increasing from 3.2 to 4.5 from 40 to 80 mL/min (3.0 to 3.6 mmol/g CO_2 adsorption capacity), then decreasing from 4.5 to 2.9 from 80 to 160 mL/min (3.6 to 3.1 mmol/g CO_2 adsorption capacity) (Figure S6, Supplementary Information). SEM image analysis showed no significant differences in crystal size or morphology between the different flow rates (Figure S13, Supplementary Information). To further evaluate the efficacy of UTSA-16(Zn) production, the CO_2 adsorption capacity production rate in mmol/h was plotted from 40 to 160 mL/min (Figure 3C). This was calculated by combining the CO_2 adsorption capacities, yields and reaction times for the individual flow rates. The results showed an overall increase in CO_2 adsorption capacity production rate from 104 to 692 mmol/h from 40 to 160 mL/min. A small peak increase in CO_2 adsorption capacity production rate from the overall trend was observed between 72 and 88 mL/min due to the enhanced adsorption capacities in this range, with CO_2 adsorption capacity at 3.6 mmol/g compared to 3.0-3.2 mmol/g at the lower (≤60 mL/min) and higher (≥100 mL/min) flow rates. The implication of these results is that despite CO_2 adsorption capacity and yield decreasing at the higher flow rates (≥100 mL/min, Figure 3B), the CO_2 adsorption capacity production rate still increases with flow rate up to at least 160 mL/min, facilitating greater scale-up possibilities. CO_2 adsorption capacity production rate is not typically calculated in the literature for comparison, though mass production rate is frequently compared as discussed below in section 3.3.

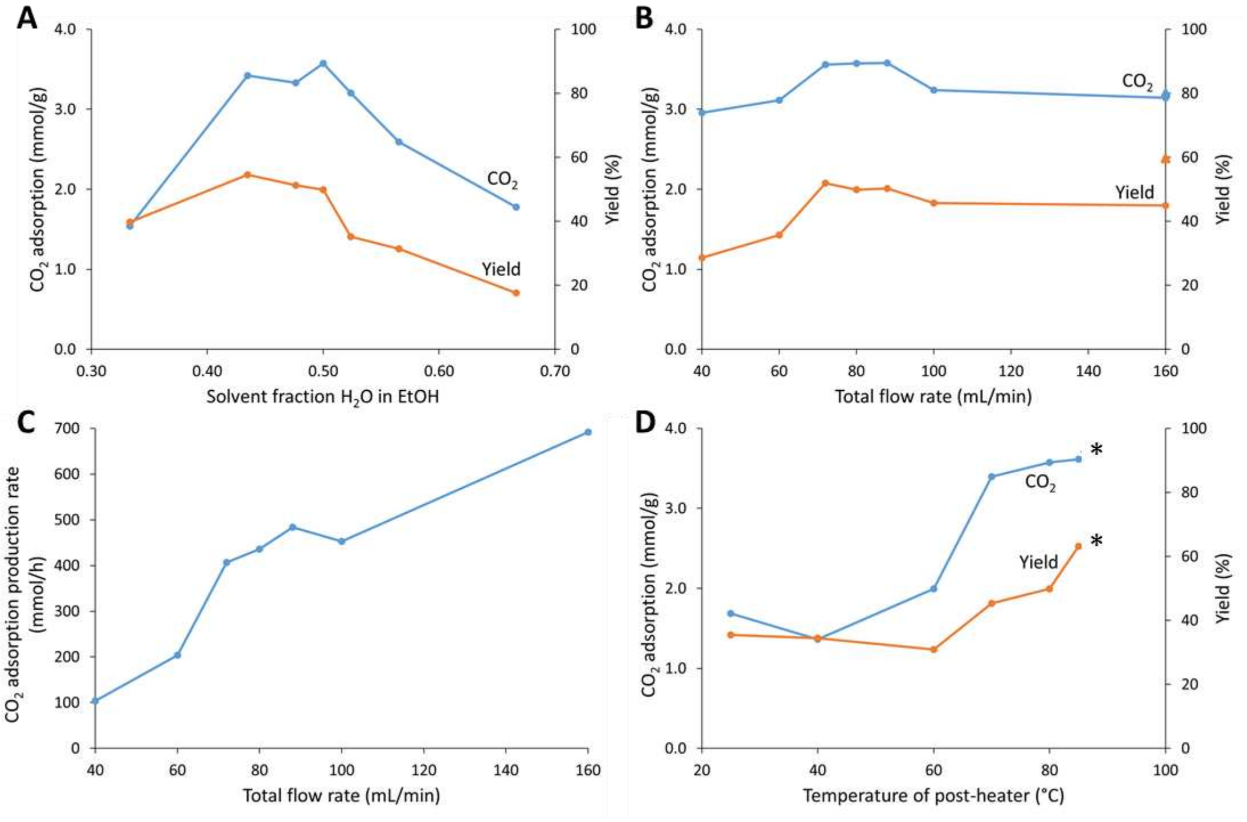

*Back-pressure regulator was used to prevent rapid solvent boiling.

Figure 3: CO_2 adsorption capacity and yield of UTSA-16(Zn) plotted against A: solvent fraction of H_2O in EtOH, B: total flow rate (triangular data points represents experiment with 160 mL/min counter-current reactor flow rate and 20 mL/min water bath heater flow rate). C: CO_2 adsorption capacity production rate of UTSA-16(Zn) plotted against flow rate. D: CO_2 adsorption capacity and yield of UTSA-16(Zn) plotted against temperature of the water bath post-heater.

Temperature is another important factor effecting MOF synthesis. Our flow rig design included a water bath heater which the reaction mixture was fed through after mixing with the antisolvent in the counter-current reactor (see Figure 1). The temperature of the bath was varied between 25 and 85 °C, and the impact on the CO_2 adsorption capacity and yield of the product were measured (Figure 3D). No major changes were observed in either metric from 25 to 60 °C. However, between 60 and 85 °C there was a steep increase in CO_2 adsorption capacity from 2.0 to 3.6 mmol/g, and MOF yield from 31% to 66% with increasing temperature. At 85 °C, a back-pressure regulator was employed to prevent solvent boil off. PXRD analyses (Figure S7, Supplementary Information) evidenced the dependence of the degree of crystallinity of UTSA-16(Zn) on temperature, with crystallinity increasing from 2.8 at 25 °C to 4.7 at 85 °C, corresponding with an increase in CO_2 adsorption capacity from 1.7 to 3.6 mmol/g. In synthesis reactions, higher temperatures result in a higher kinetic energy of the reactants, enabling them to overcome the activation energy and resulting in shorter reaction times, as observed with MOF-5[71]. Syntheses performed at higher temperatures also tend to lead to denser structures with higher degrees of framework connectivity and lower levels of solvation[72], and support the formation of more thermodynamically favoured structures, as demonstrated with various Zn and Cu-based MOFs[73,74]. Higher degrees of crystallinity are typically thermodynamically favoured[75], so more crystalline materials are usually produced at higher reaction temperatures. This is supported by our results and a study on the mixed-metal MOF UTSA-16(Co,Zn), where lower temperature (≤60 °C) produced primarily amorphous products, with improved crystallinity at temperatures ≥80 °C[11]. Higher temperatures can also enable sufficient energy for reorganisation of an initially disordered MOF structure, leading to the more thermodynamically stable and ordered crystalline structure. This procedure has been reported with MOF UiO-66-NH_2, where a two-step process with heating led to reorganisation of the framework structure to increase crystallinity[76].

3.3 Impact of scaling-up synthesis on yield and CO_2 adsorption capacity

Optimisation of the chemical and physical parameters were conducted by continuously collecting products over a timescale in which roughly 1 g of MOF was collected. To test the initial scope for scale-up, the reaction was continued for 10-fold the duration, approximately 10 g scale (see experimental section). The CO_2 adsorption capacity was approximately the same (3.6 mmol/g) for the 1 g and 10 g scale reactions, as expected (Figure S10A, Supplementary Information). The yield showed an increase from 50% to 59% from 1 g to 10 g scale, likely from reduced loses during collection. PXRD patterns show no significant differences in the degree of crystallinity between the 1 g and 10 g scale reactions (Figure S8, Supplementary Information), and SEM images show a similar morphology for both scales, consisting mostly of 50-100 nm approximately octahedral polyhedra (Figure S14, Supplementary Information). These results demonstrate the reliability and consistency of the flow process developed herein for producing UTSA-16(Zn).

For UTSA-16(Zn) (10 g scale), recyclability of the CO_2 adsorption-desorption capabilities of the MOF was measured over 12 cycles (Figure S10B, Supplementary Information). A low regeneration temperature of 60 °C was used for CO_2 desorption during the cycling to measure recyclability with low-energy regeneration, in line with our previous study[20]. CO_2 adsorption capacity measured after regeneration was lower for UTSA-16(Zn) regenerated at 60 °C (3.3 mmol/g) compared to 150 °C (3.6 mmol/g); however, no decrease of CO_2 adsorption capacity was detected over the 12 cycles (cycle 1: 3.23 mmol/g, cycle 12: 3.29 mmol/g). This contrasts with the decreasing CO_2 capacity observed for some other materials such as an amine-based adsorbent (7% decrease over 19 cycles)[77] and zeolite Y templated carbon (6% decrease over 5 cycles)[78], due to incomplete regeneration between cycles.

Key performance metrics for scale-up are production rate (g/h) and space time yield (STY, kg/m^3/day)[79]. Our 10 g scale reaction demonstrated a production rate of 173 g/h and an STY of 23,573 kg/m^3/day (24 h), treating the reaction as part of a continuous synthesis (*i.e* excluding set-up/shutdown time) and using the heating coil as the reactor volume[68]. This represents a 77-fold increase in production rate and a 15-fold increase in STY for UTSA-16(Zn) compared to the previously highest reported (microwave batch process, production rate: 2.25 g/h, STY: 1543 kg/m^3/day)[20], demonstrating the benefits of continuous flow synthesis. Production rate is considered a more representative metric for comparing MOF flow syntheses, as STYs are prone to over-extrapolation and have high variation based on how the reactor or reaction mixture volume is calculated[68,79,80]. Typical STY values for MOF flow syntheses are between 400 and 10,000 kg/m^3/day[18,79], though values as high as 6.32 x 10^5 have been reported[19]. Successful scale-up of production rate using flow-syntheses of other MOFs and a variety of reactor designs has also been reported, including HKUST-1 (60 g/h)[17], MIL-53(Al) (125 g/h)[40], UiO-66 (104 g/h)[81], CPO-27(Ni) (132 g/h)[39], and ZIF-8 (27 g/h lab scale, 810 g/h pilot scale reactor)[38]. Based on similar published reactor design to ours at a larger scale, transfer from our lab-scale flow reactor to a larger pilot-scale reactor would also likely be possible for further scale-up of production rate[38].

As described in the experimental section, our standard collection and washing/activation protocol for UTSA-16(Zn) involved collecting the powder product by centrifuge, washing three times with methanol and drying in an oven overnight. To see if further washing of UTSA-16(Zn) would impact the CO_2 adsorption capacity, a small aliquot of the 10 g scale reaction (0.8 g) was separated before drying and subject to a further 6 methanol washing steps with solvent exchange over 5 days. The extra washing steps resulted in an increase from 3.6 to 3.8 mmol/g CO_2 adsorption capacity (Figure S10A, Supplementary Information). This increase shows that UTSA-16(Zn) is not fully activated during the standard washing procedure, and further improvements to the CO_2 adsorption capacity can be made through optimisation of the washing/activation procedure. However, if additional solvent, time, and energy (e.g. vacuum drying or drying solvents) are required for these improvements, as have been used previously for UTSA-16(Zn)[11,12], due consideration must be given to the negative impacts on the sustainability and scalability of the manufacturing process[13]. For instance, in the extra washing case, a 267% increase in solvent quantity and an additional 5 days of solvent soaking time were required to achieve only a 6% increase in CO_2 adsorption capacity. There are no differences in crystallinity or morphology of UTSA-16(Zn) (Figures S8, S14, Supplementary Information) because of the washing steps. The increase in CO_2 adsorption capacity is therefore attributed to the further removal of water/solvent molecules from the MOF pores[82].

3.4 Incorporation of Fe_3O_4 into UTSA-16(Zn)

As discussed in the introduction, incorporation of magnetic nanoparticles into MOFs, forming MFCs, enables rapid and energy efficient induction heating for MFC regeneration for reuse[83].

Herein, we successfully synthesised MFCs at a production rate of 152 g/h by adapting the continuous flow method developed for UTSA-16(Zn) to incorporate the citrate-coated Fe_3O_4 (see experimental section 2.5). A citrate coating was selected to prevent agglomeration of the Fe_3O_4 MNPs and to enhance chemical interactions between the MNPs and the UTSA-16(Zn), which contains citrate anions as the linker molecules of the MOF. This production rate represents the highest reported for any MFC to-date (previous highest of 13 g/h for $MgFe_2O_4$@UiO-66-NH_2)[84]. MFCs synthesised herein contain 2.9 and 11.4 wt% MNP-CA, quantified through saturation magnetisation measurements[27] (Figure 4A). These values are close to those previously reported in our group using a microwave batch method[20] and other reported MFCs, such as 0.1-7.8 wt% Fe_3O_4 in Mg-MOF-74[85], 2.0-4.1 wt% $MgFe_2O_4$ in UiO-66[26] and 1.3-7.3 wt% Fe_3O_4 in PCN-250[86].

Figure 4B shows the impact of MNP-CA incorporation into UTSA-16(Zn) on CO_2 adsorption capacity and yield. The yield was shown to be unaffected by composite formation, remaining around 50% for both UTSA-16(Zn)@MNP-CA MFCs. This value is higher than observed elsewhere for the flow synthesis of an MFC, such as 18-34% for $MgFe_2O_4$@UiO-66-NH_2[84]. The CO_2 adsorption capacity decreased with increasing MNP-CA content, from 3.6 to 3.1 mmol/g from 0 to 11.4 wt.% MNP-CA. This decrease is expected as MNP-CA does not adsorb CO_2. However, accounting for the mass of MNP-CA in the MFCs, the CO_2 capacity of the UTSA-16(Zn) did not decrease, but remained around 3.6 mmol/g. This demonstrates that MNP-CA incorporation had no detrimental impact on MOF synthesis or CO_2 capacity, which could have occurred due to pore blocking effects[87,88].

The impact on N_2 adsorption isotherms and apparent BET surface area of MNP-CA in UTSA-16(Zn)@MNP-CA (11.4%) compared to UTSA-16(Zn) was evaluated (Figure 4E). The adsorption isotherms demonstrated Type 1 isotherms due to the microporous structures, matching those reported for UTSA-16(Zn)[11,12]. Surface areas were similar to those previously reported for the MOF (787 m^2/g)[12] and MFC (590 m^2/g)[20]: 743 m^2/g for UTSA-16(Zn) and 637 m^2/g for UTSA-16(Zn)@MNP-CA (11.4%). CO_2 adsorption isotherms were also measured for UTSA-16(Zn) and UTSA-16(Zn)@MNP-CA (11.4%) at 273 K and 298 K (Figure 4F). The volumetric CO_2 isotherms also matched the Type 1 adsorption behaviour previously reported for UTSA-16(Zn)[11,12]. As expected, the higher temperature CO_2 isotherms (298 K) for UTSA-16(Zn) and UTSA-16(Zn)@MNP-CA (11.4 %) showed a slower rate of adsorption and lower overall adsorption compared to the lower temperature isotherms (273 K)[89]. The total uptakes were also as expected for the MOF and MFC, corroborating our gravimetric measurements reported above: 3.6 mmol/g for UTSA-16(Zn) and 3.1 mmol/g for UTSA-16(Zn)@MNP-CA (11.4%) at 1 bar CO_2.

Isosteric heats of adsorption were around 30-35 kJ/mol for both materials (Figure S12, Supplementary Information), consistent with that observed for UTSA-16(Zn)[11] with no significant differences between the MFC and the MOF.

The CO_2 adsorption-desorption recyclability of UTSA-16(Zn)@MNP-CA (11.4%) was measured over 12 cycles (Figure 4D), as performed on the pristine MOF in section 3.3 and Figure S10B, Supplementary Information. A regeneration temperature of 60 °C was used for the CO_2 desorption steps, which again resulted in a slight decrease in CO_2 adsorption capacity compared to 150 °C (3.1 mmol/g for 150 °C, 2.9 mmol/g for 60 °C). As with pristine UTSA-16(Zn) in section 3.3, there was no decrease in the CO_2 adsorption capacity over the 12 cycles (cycle 1: 2.89 mmol/g, cycle 12: 2.89 mmol/g). In addition, MNP-CA incorporation has no negative impact on the thermal stability of UTSA-16(Zn), since all UTSA16(Zn)@MNP-CA MFCs were thermally stable up to 250 °C, akin to the pristine MOF (Figure S11, Supplementary Information).

Overall, CO_2 adsorption capacities obtained for UTSA-16(Zn) and UTSA16(Zn)@MNP-CA MFCs (3.1-3.8 mmol/g) were comparable to those previously reported for pristine UTSA-16(Zn) (3.5 mmol/g for conventionally heated solvothermal[11] and 3.4 mmol/g for microwave[20] batch methods) and other high performing MOFs/MOF composites[90,91]. The absolute maximum reported CO_2 adsorption capacity for pristine UTSA-16(Zn) is 4.7 mmol/g, via a 4 h microwave batch method, though this required 14 washes over 3 days with anhydrous diethyl ether and methanol and 90 °C vacuum drying[12]. Advantages in the route reported herein are a substantial improvement toward the sustainability and scalability of the MOF/MFC synthesis, including the low-cost and scalable flow synthesis route, short washing/activation procedure (3 washes with standard commercial MeOH over 1 h, 50 °C drying without a vacuum), high production rate, and capability for magnetic induction heating for localised low-energy regeneration. PXRD measurements confirmed the presence and crystallinity of both the MOF and MNP-CA components in the UTSA16(Zn)@MNP-CA MFCs, with Fe_3O_4 peaks at 30, 36 and 43 °2θ representing the MNP-CA[20] (Figure S9, Supplementary Information). Distribution of MNP-CA in UTSA-16(Zn) was probed using MLA with EDS elemental analysis (Figure S15, Supplementary Information). Previous investigation discussed the correlation between MLA and XRD in the formation of perovskite-type structural phases, highlighting that whereas XRD enables the detection of crystallographic phases, MLA can provide information on chemical concentrations and distributions[92]. MNP-CA was well dispersed amongst the UTSA-16(Zn), allowing effective induction heating throughout the material even with a high wt.% MOF loading (89-97%), maximising gravimetric CO_2 adsorption capacity. These MFC structures are distinct from other nanoparticle-containing MFCs reported in the literature, for instance thin MOF layers grown on individual nanoparticles such as HKUST-1 on Fe_3O_4[93,94] and ZIF-8 on Fe_3O_4[95]. These core-shell structures typically have much lower wt.% MOF loadings in the composites[93,94] and require many preparation steps such as layer-by-layer syntheses. The UTSA-16(Zn)@MNP-CA structure is also distinct from MFCs grown via slow direct-growth methods, where large MOF crystals grow around nanoparticles. Examples of these structures include $MgFe_2O_4$ in Mg-MOF-74[27] or Fe_3O_4 in Co-MOF-74[96], formulated over 15 h and 2.5 day syntheses, respectively.

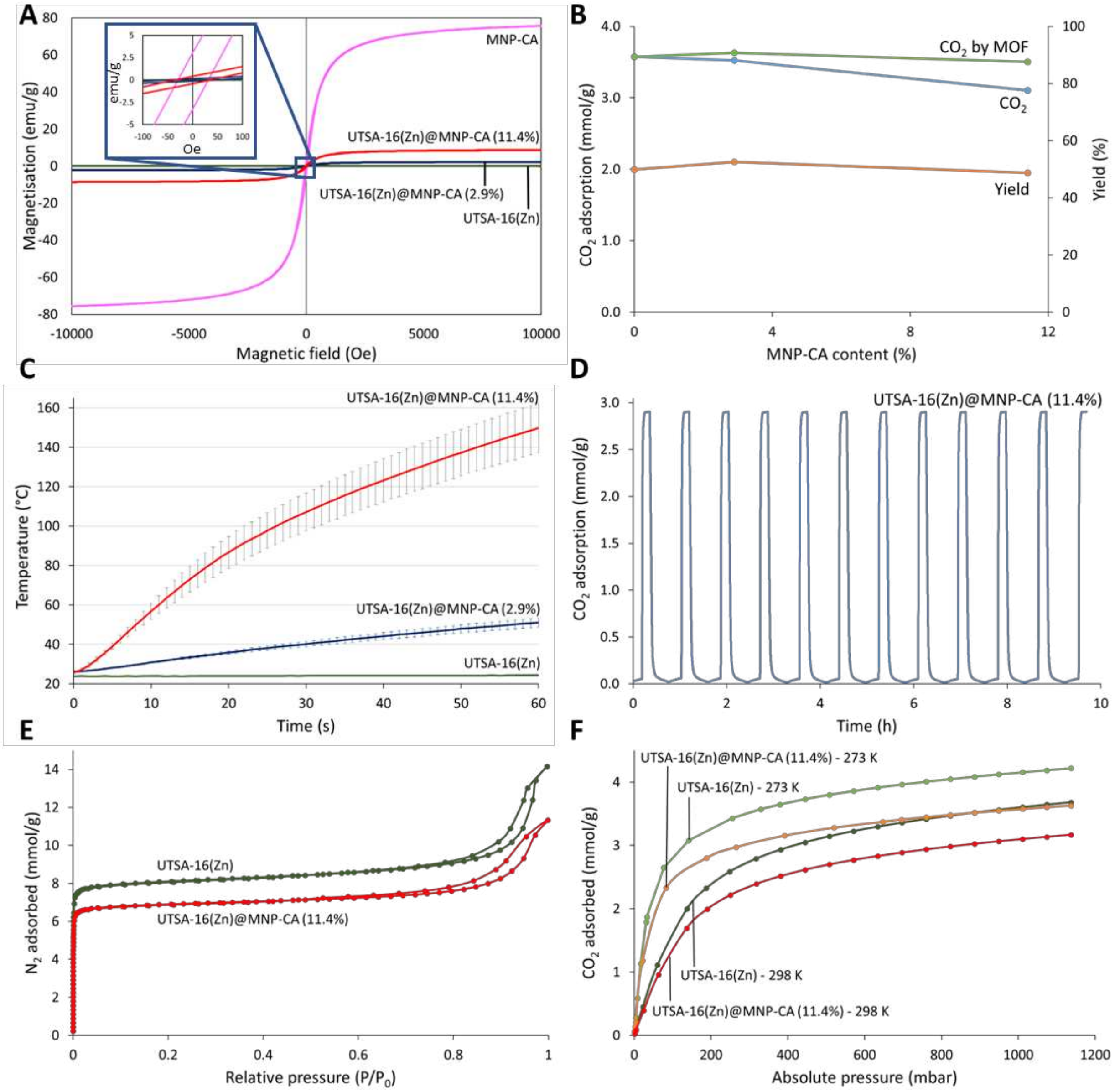

Figure 4: A: room temperature magnetisation measurements of UTSA-16(Zn), MNP-CA and UTSA 16(Zn)@MNP-CA MFCs, with a field strength up to 10 kOe. B: CO_2 adsorption capacity and yield of UTSA-16(Zn)@MNP-CA plotted against MNP-CA content. C: Temperature reached by induction heating over 30 s at 500 W for UTSA-16(Zn) and UTSA 16(Zn)@MNP-CA MFCs. Results are an average over 3 experiments with error bars showing ±1 standard deviation. D: CO_2 adsorption and desorption (60 °C) of UTSA-16(Zn)@MNP-CA (11.4%) over 12 cycles. E: N_2 adsorption isotherms at 77 K of UTSA-16(Zn) and UTSA-

16(Zn)@MNP-CA (11.4 %). F: CO_2 adsorption isotherms of UTSA-16(Zn) and UTSA-16(Zn)@MNP-CA (11.4 %), measured at 273 K and 298 K.

The saturation magnetisation properties of the MFCs were measured by VSM analyses to be 2.2 and 8.6 emu/g for UTSA-16(Zn)@MNP-CA (2.9%) and UTSA-16(Zn)@MNP-CA (11.4%), respectively (Figure 4A). This is within the ranges reported for other MFCs, such as 1.5-4 emu/g for $MgFe_2O_4$ in UiO66[26], 0.1-3.9 emu/g for Fe_3O_4 in Mg-MOF-74[85] and 3.1-18.4 emu/g for Fe_3O_4 in PCN-250[86]. For comparison, pristine UTSA-16(Zn) and MNP-CA had saturation magnetisations of 0.0 and 75.7 emu/g, respectively. Induction heating tests were conducted for the pristine MOF and MFCs at 500 W over a 60 s period (magnetic field: 164 A/m), results shown in Figure 4C. As anticipated, pristine UTSA-16(Zn) showed no heating over the time period, and the higher MNP-CA concentration in the MFC resulted in a much faster heating rate than the lower concentration (26-150 °C in 60 s for UTSA-16(Zn)@MNP-CA (11.4%) and 26-51 °C in 60 s for UTSA-16(Zn)@MNP-CA (2.9%)).

A balance between CO_2 adsorption capacity and induction heating rate can be achieved when considering the optimal concentration of MNP-CA in the MFC, which may vary depending on the application environment. As shown in Figure 4D, temperatures as low as 60 °C resulted in effective desorption in repeated adsorption-desorption cycling without loss of capacity for UTSA-16(Zn)@MNP-CA. This is much lower than temperatures typically required for other adsorbents such as zeolites (200 °C)[97], carbon-based materials (120-230 °C)[98], and other MFCs (130-145 °C)[27]. Furthermore, due to the efficiency of the magnetic induction heating method, temperatures required for the desorption step were reached in seconds (e.g. 60 °C in 11 s for UTSA-16(Zn)@MNP-CA (11.4%), Figure 4C). Typical regeneration times range between 20-40 min for alternate adsorbents such as activated carbon and zeolites using conventional or microwave heating[99,100], and previous MFCs have demonstrated regeneration times as fast as 4-11 min via magnetic induction heating[26,27,101].

This work shows that the MOF UTSA-16(Zn) and MFCs containing UTSA-16(Zn) and MNP-CA can be synthesised through a rapid and sustainable continuous flow process, benefiting from high production rates (173 g/h for UTSA-16(Zn) and 152 g/h for the MFCs), high CO_2 adsorption capacities (3.1-3.8 mmol/g) and effective thermal regeneration at temperatures as low as 60 °C, which were attained in seconds for the MFCs via the energy efficient induction heating process.

4 Conclusions

Herein we report the first continuous flow synthesis of promising CO_2 capture MOF UTSA-16(Zn). A high production rate (173 g/h) and STY (23573 kg/m^3/day) were achieved compared to the batch synthesis (2.25 g/h, 1543 kg/m^3/day), representing a 77-fold and 15-fold increase respectively. The lab-scale reactor design is scalable, and higher flow rates resulted in higher CO_2 adsorption capacity production rates (692 mmol/h at 160 mL/min). The procedure developed herein marks a significant step towards industrial application for UTSA-16(Zn), maximising reaction sustainability through low-cost and non-toxic reagents and a low-energy atmospheric pressure flow reactor.

A detailed optimisation study identified key variables and their impacts on the CO_2 adsorption capacity and product yield metrics of the MOF. The optimal Zn:L:B reagent ratio was 1:1:3 (3.6 mmol/g, 50% yield), with further increases to the L and B concentrations improving the CO_2 capacity at the expense of the yield (3.8 mmol/g, 24% yield at 1:1.2:3.6 Zn:L:B). CO_2 adsorption capacity increased with an optimum concentration of incorporated

Mg (3.8 mmol/g at 0.018 Mg metal mole fraction in product), though only approx. 8% of the added Mg was incorporated, with associated losses to the overall yield (35%).

Both CO_2 adsorption capacity and yield were very sensitive to the H_2O:EtOH solvent ratio; a 1:1 ratio gave the best results (3.6 mmol/g, 50% yield). The optimal reactor mixing efficiency to maximise CO_2 adsorption capacity was at an 80 mL/min flow rate (3.6 mmol/g), and the yield was further improved (up to 60%) using a lower flow rate (20 mL/min, longer residence time) through the coil heater. Both CO_2 adsorption capacity and yield improved with higher heating temperatures (from 1.7 mmol/g, 35% yield at 25 °C up to 3.6 mmol/g, 63% yield at 85 °C), though a back-pressure regulator was required above 80 °C to prevent solvent boil-off. A 10-fold increase in reaction size (from 1 g to 10 g scale) increased the yield (59% at 10 g scale compared to 50% at 1 g scale) and a high CO_2 adsorption capacity was maintained (3.6 mmol/g). Additional washing and soaking MOF in solvent showed that further increases to CO_2 capacity were possible (3.8 mmol/g) however this is at the expense of sustainability.

Finally, citrate-coated Fe_3O_4 magnetic nanoparticles were added into the flow synthesis of UTSA-16(Zn), producing MFCs with 2.9 and 11.4 wt.% incorporated MNP-CA. No detrimental effects were observed for yield (≈50%), CO_2 adsorption capacity of the MOF component (≈3.6 mmol/g), or recyclability (no loss in CO_2 capacity over 12 cycles). Saturation magnetisations of 2.2 and 8.6 emu/g were measured for UTSA-16(Zn)@MNP-CA (2.9%) and UTSA-16(Zn)@MNP-CA (11.4%), respectively. The MFCs demonstrated rapid heating under a magnetic field (26-150 °C in 60 s for UTSA-16(Zn)@MNP-CA (11.4%)), highly beneficial for material regeneration for reuse. This represents the largest production rate of any reported MFC to date (152 g/h) and demonstrates the scalability of this novel class of materials.

The flow synthesis method developed herein will facilitate the transfer of UTSA-16(Zn) and UTSA-16(Zn)@MNP-CA production to pilot-scale reactors, enabling larger-scale testing of the materials in CO_2 capture application environments. The methods developed will also aid in the discovery and understanding of other MOFs/MFCs, supporting their transition to larger scale manufacture and broad industrial applications.

5 Author contributions

John Luke Woodliffe: Investigation, Methodology, Conceptualization, Formal Analysis, Validation, Visualization and Writing – Original Draft, Review & Editing. Jesús Molinar-Díaz: Investigation (mineral liberation analysis), Writing – Original Draft and Visualization. Rob Clowes: Investigation (adsorption isotherms). Oday Hussein: Investigation (vibrating sample magnetometry). Ed Lester: Resources. Rebecca Ferrari: Conceptualization. Ifty Ahmed: Supervision, Conceptualization, and Writing – Review & Editing. Andrea Laybourn: Supervision, Conceptualization, Project Administration, Writing – Review & Editing, and Funding Acquisition.

6 Conflicts of interest

The authors declare no conflicts of interest.

7 Acknowledgements

Funding: The authors thank and acknowledge the Engineering and Physical Sciences Research Council (EPSRC) and Science Foundation Ireland (SFI) Centre for Doctoral Training in Sustainable Chemistry: Atoms-2-Products an Integrated Approach to Sustainable Chemistry [Grant number: EP/S022236/1].

The authors thank the Royce Discovery Centre, University of Sheffield for access to QD MPMS 3 facilities; EPSRC Grant Number EP/R00661X/1 & EP/P02470X/1. SEM analyses were supported by the EPSRC (EP/L022494/1) and the University of Nottingham. MLA/EDS analyses were supported by the EPSRC (EP/P006701/1), as part of the "EPSRC Future Composites Manufacturing Research Hub". The authors acknowledge the Nanoscale and Microscale Research Centre at the University of Nottingham for access to SEM instrumentation. The authors also thank Amy-Louise Johnston and Vikki Archibald (both University of Nottingham) for assisting with manufacture of the Fe_3O_4 nanoparticles, and for performing ICP-OES analyses, respectively.

8 References

(1) Global CCS Institute. *The Global Status of CCS: 2019*; Australia, 2019.

(2) Sjostrom, S.; Krutka, H. Evaluation of Solid Sorbents as a Retrofit Technology for CO2 Capture. *Fuel* **2010**, *89* (6), 1298–1306. https://doi.org/https://doi.org/10.1016/j.fuel.2009.11.019.

(3) Li, X.; Wang, S.; Chen, C. Experimental Study of Energy Requirement of CO2 Desorption from Rich Solvent. *Energy Procedia* **2013**, *37*, 1836–1843. https://doi.org/10.1016/j.egypro.2013.06.063.

(4) Yuan, B.; Zhan, G.; Chen, Z.; Li, Y.; Wang, L.; You, C.; Li, J. Intrinsic Insight of Energy-Efficiency Optimization for CO2 Capture by Amine-Based Solvent: Effect of Mass Transfer and Solvent Regeneration. *International Journal of Greenhouse Gas Control* **2022**, *118*, 103673. https://doi.org/https://doi.org/10.1016/j.ijggc.2022.103673.

(5) Bochon, K.; Chmielniak, T. Energy and Economic Analysis of the Carbon Dioxide Capture Installation with the Use of Monoethanolamine and Ammonia. *Archives of Thermodynamics*. The Committee of Thermodynamics and Combustion of the Polish Academy of Sciences and The Institute of Fluid-Flow Machinery Polish Academy of Sciences 2015, pp 93–110. https://doi.org/10.1515/aoter-2015-0007.

(6) Markewitz, P.; Kuckshinrichs, W.; Leitner, W.; Linssen, J.; Zapp, P.; Bongartz, R.; Schreiber, A.; Müller, T. E. Worldwide Innovations in the Development of Carbon Capture Technologies and the Utilization of CO2. *Energy Environ Sci* **2012**, *5* (6), 7281. https://doi.org/10.1039/c2ee03403d.

(7) Farmahini, A. H.; Krishnamurthy, S.; Friedrich, D.; Brandani, S.; Sarkisov, L. Performance-Based Screening of Porous Materials for Carbon Capture. *Chem Rev* **2021**. https://doi.org/10.1021/acs.chemrev.0c01266.

(8) Samanta, A.; Zhao, A.; Shimizu, G. K. H.; Sarkar, P.; Gupta, R. Post-Combustion CO2 Capture Using Solid Sorbents: A Review. *Ind Eng Chem Res* **2012**, *51* (4), 1438–1463. https://doi.org/10.1021/ie200686q.

(9) Yaghi, O. M.; Li, H. Hydrothermal Synthesis of a Metal-Organic Framework Containing Large Rectangular Channels. *J Am Chem Soc* **1995**, *117* (41), 10401–10402. https://doi.org/10.1021/ja00146a033.

(10) Ding, M.; Flaig, R. W.; Jiang, H.-L.; Yaghi, O. M. Carbon Capture and Conversion Using Metal–Organic Frameworks and MOF-Based Materials. *Chem Soc Rev* **2019**, *48* (10), 2783–2828. https://doi.org/10.1039/C8CS00829A.

(11) Peh, S. B.; Xi, S.; Karmakar, A.; Yeo, J. Y.; Wang, Y.; Zhao, D. Accelerated Formation Kinetics of a Multicomponent Metal–Organic Framework Derived from Preferential Site Occupancy. *Inorg Chem* **2020**, *59* (13), 9350–9355. https://doi.org/10.1021/acs.inorgchem.0c01226.

(12) Gaikwad, S.; Kim, S.-J.; Han, S. Novel Metal–Organic Framework of UTSA-16 (Zn) Synthesized by a Microwave Method: Outstanding Performance for CO2 Capture with Improved Stability to Acid Gases. *Journal of Industrial and Engineering Chemistry* **2020**, *87*, 250–263. https://doi.org/https://doi.org/10.1016/j.jiec.2020.04.015.

(13) Woodliffe, J. L.; Ferrari, R. S.; Ahmed, I.; Laybourn, A. Evaluating the Purification and Activation of Metal-Organic Frameworks from a Technical and Circular Economy Perspective. *Coord Chem Rev* **2021**, *428*, 213578. https://doi.org/10.1016/j.ccr.2020.213578.

(14) Rubio-Martinez, M.; Avci-Camur, C.; Thornton, A. W.; Imaz, I.; Maspoch, D.; Hill, M. R. New Synthetic Routes towards MOF Production at Scale. *Chem Soc Rev* **2017**, *46* (11), 3453–3480. https://doi.org/10.1039/C7CS00109F.

(15) Laybourn, A.; Robertson, K.; Slater, A. G. Quid Pro Flow. *J Am Chem Soc* **2023**, *145* (8), 4355–4365. https://doi.org/10.1021/jacs.2c13670.

(16) Dunne, P. W.; Lester, E.; Walton, R. I. Towards Scalable and Controlled Synthesis of Metal–Organic Framework Materials Using Continuous Flow Reactors. *React Chem Eng* **2016**, *1* (4), 352–360. https://doi.org/10.1039/C6RE00107F.

(17) Rubio-Martinez, M.; Batten, M. P.; Polyzos, A.; Carey, K.-C.; Mardel, J. I.; Lim, K.-S.; Hill, M. R. Versatile, High Quality and Scalable Continuous Flow Production of Metal-Organic Frameworks. *Sci Rep* **2014**, *4*, 5443. https://doi.org/10.1038/srep05443.

(18) Batten, M. P.; Rubio-Martinez, M.; Hadley, T.; Carey, K. C.; Polyzos, K. S. L. A.; Hill, M. R. Continuous Flow Production of Metal-Organic Frameworks. *Curr Opin Chem Eng* **2015**, *8*, 55–59. https://doi.org/10.1016/j.coche.2015.02.001.

(19) Laybourn, A.; López-Fernández, A. M.; Thomas-Hillman, I.; Katrib, J.; Lewis, W.; Dodds, C.; Harvey, A. P.; Kingman, S. W. Combining Continuous Flow Oscillatory Baffled Reactors and Microwave Heating: Process Intensification and Accelerated Synthesis of Metal-Organic Frameworks. *Chemical Engineering Journal* **2019**, *356*, 170–177. https://doi.org/10.1016/j.cej.2018.09.011.

(20) Woodliffe, J. L.; Johnston, A.-L.; Fay, M.; Ferrari, R.; Gomes, R. L.; Lester, E.; Ahmed, I.; Laybourn, A. Rapid Microwave Synthesis of Sustainable Magnetic Framework Composites of UTSA-16(Zn) with Fe 3 O 4 Nanoparticles for Efficient CO 2 Capture. *Mater Adv* **2023**, *4* (22), 5838–5849. https://doi.org/10.1039/D3MA00351E.

(21) Huang, B. L.; Ni, Z.; Millward, A.; McGaughey, A. J. H.; Uher, C.; Kaviany, M.; Yaghi, O. Thermal Conductivity of a Metal-Organic Framework (MOF-5): Part II. Measurement. *Int J Heat Mass Transf* **2007**, *50* (3), 405–411. https://doi.org/https://doi.org/10.1016/j.ijheatmasstransfer.2006.10.001.

(22) Ma, Y. J.; Jiang, X. X.; Lv, Y. K. Recent Advances in Preparation and Applications of Magnetic Framework Composites. *Chem Asian J* **2019**, *14* (20), 3515–3530. https://doi.org/10.1002/asia.201901139.

(23) Yadav, S.; Dixit, R.; Sharma, S.; Dutta, S.; Solanki, K.; Sharma, R. K. Magnetic Metal–Organic Framework Composites: Structurally Advanced Catalytic Materials for Organic Transformations. *Mater Adv* **2021**, *2* (7), 2153–2187. https://doi.org/10.1039/D0MA00982B.

(24) Woodliffe, J. L.; Molinar-Díaz, J.; Islam, M. T.; Stevens, L. A.; Wadge, M. D.; Rance, G. A.; Ferrari, R.; Ahmed, I.; Laybourn, A. Rapid Synthesis of Magnetic Microspheres and the Development of New Macro–Micro Hierarchically Porous Magnetic Framework Composites. *J Mater Chem A Mater* **2023**. https://doi.org/10.1039/D3TA01927F.

(25) Rudnev, V.; Loveless, D.; Cook, R. L. *Handbook of Induction Heating*; CRC Press, 2017. https://doi.org/10.1201/9781315117485.

(26) Sadiq, M. M.; Li, H.; Hill, A. J.; Falcaro, P.; Hill, M. R.; Suzuki, K. Magnetic Induction Swing Adsorption: An Energy Efficient Route to Porous Adsorbent Regeneration. *Chemistry of Materials* **2016**, *28* (17), 6219–6226. https://doi.org/10.1021/acs.chemmater.6b02409.

(27) Sadiq, M. M.; Konstas, K.; Falcaro, P.; Hill, A. J.; Suzuki, K.; Hill, M. R. Engineered Porous Nanocomposites That Deliver Remarkably Low Carbon Capture Energy Costs. *Cell Rep Phys Sci* **2020**, *1* (6), 100070. https://doi.org/10.1016/j.xcrp.2020.100070.

(28) Gholami, M.; Verougstraete, B.; Vanoudenhoven, R.; Baron, G. V.; Van Assche, T.; Denayer, J. F. M. Induction Heating as an Alternative Electrified Heating Method for Carbon Capture Process. *Chemical Engineering Journal* **2022**, *431* (October 2021), 133380. https://doi.org/10.1016/j.cej.2021.133380.

(29) Newport, K.; Baamran, K.; Rownaghi, A. A.; Rezaei, F. Magnetic-Field Assisted Gas Desorption from Fe2O3/Zeolite 13X Sorbent Monoliths for Biogas Upgrading. *Ind Eng Chem Res* **2022**, *61* (51), 18843–18853. https://doi.org/10.1021/acs.iecr.2c02969.

(30) Maity, R.; Gholami, M.; Peter, S. A.; Schoukens, M.; Tiriana, S.; Baron, G. V.; Denayer, J. F. M. Strategic Fast Induction Heating to Combat Hysteresis Barriers in a Flexible MOF for Rapid CO2 Desorption in Biogas Upgrading. *Small* **2023**, *2302893*, 1–5. https://doi.org/10.1002/smll.202302893.

(31) Baamran, K.; Newport, K.; Rownaghi, A. A.; Rezaei, F. Development and Assessment of Magnetic Fe2O3@MOF-74 Composite Sorbents for Ethylene/Ethane Separation. *Chemical Engineering Journal* **2023**, *451*, 139006. https://doi.org/10.1016/j.cej.2022.139006.

(32) Grande, C. A.; Blom, R.; Middelkoop, V.; Matras, D.; Vamvakeros, A.; Jacques, S. D. M.; Beale, A. M.; Di Michiel, M.; Anne Andreassen, K.; Bouzga, A. M. Multiscale Investigation of Adsorption Properties of Novel 3D Printed UTSA-16 Structures. *Chemical Engineering Journal* **2020**, *402* (May), 126166. https://doi.org/10.1016/j.cej.2020.126166.

(33) Grande, C. A.; Rodrigues, A. E. Electric Swing Adsorption for CO2 Removal from Flue Gases. *International Journal of Greenhouse Gas Control* **2008**, *2* (2), 194–202. https://doi.org/10.1016/S1750-5836(07)00116-8.

(34) Gaikwad, R.; Gaikwad, S.; Han, S. Bimetallic UTSA-16 (Zn, X; X = Mg, Mn, Cu) Metal Organic Framework Developed by a Microwave Method with Improved CO2capture Performances. *Journal of Industrial and Engineering Chemistry* **2022**, *111*, 346–355. https://doi.org/10.1016/j.jiec.2022.04.016.

(35) Gates-Rector, S.; Blanton, T. The Powder Diffraction File: A Quality Materials Characterization Database. *Powder Diffr* **2019**, *34* (4), 352–360. https://doi.org/10.1017/S0885715619000812.

(36) Plaza, M. G.; Pevida, C.; Arias, B.; Fermoso, J.; Arenillas, A.; Rubiera, F.; Pis, J. J. Application of Thermogravimetric Analysis to the Evaluation of Aminated Solid Sorbents for CO2 Capture. *J Therm Anal Calorim* **2008**, *92* (2), 601–606. https://doi.org/10.1007/s10973-007-8493-x.

(37) Lester, E.; Blood, P.; Denyer, J.; Giddings, D.; Azzopardi, B.; Poliakoff, M. Reaction Engineering: The Supercritical Water Hydrothermal Synthesis of Nano-Particles. *J Supercrit Fluids* **2006**, *37* (2), 209–214. https://doi.org/https://doi.org/10.1016/j.supflu.2005.08.011.

(38) Munn, A. S.; Dunne, P. W.; Tang, S. V. Y.; Lester, E. H. Large-Scale Continuous Hydrothermal Production and Activation of ZIF-8. *Chemical Communications* **2015**, *51* (64), 12811–12814. https://doi.org/10.1039/C5CC04636J.

(39) Gimeno-Fabra, M.; Munn, A. S.; Stevens, L. A.; Drage, T. C.; Grant, D. M.; Kashtiban, R. J.; Sloan, J.; Lester, E.; Walton, R. I. Instant MOFs: Continuous Synthesis of Metal–Organic Frameworks by Rapid Solvent Mixing. *Chemical Communications* **2012**, *48* (86), 10642. https://doi.org/10.1039/c2cc34493a.

(40) Bayliss, P. A.; Ibarra, I. A.; Pérez, E.; Yang, S.; Tang, C. C.; Poliakoff, M.; Schröder, M. Synthesis of Metal–Organic Frameworks by Continuous Flow. *Green Chemistry* **2014**, *16* (8), 3796–3802. https://doi.org/10.1039/C4GC00313F.

(41) Taddei, M.; Casati, N.; Steitz, D. A.; Dümbgen, K. C.; van Bokhoven, J. A.; Ranocchiari, M. In Situ High-Resolution Powder X-Ray Diffraction Study of UiO-66 under Synthesis Conditions in a Continuous-Flow Microwave Reactor. *CrystEngComm* **2017**, *19* (23), 3206–3214. https://doi.org/10.1039/C7CE00867H.

(42) Seetharaj, R.; Vandana, P. V.; Arya, P.; Mathew, S. Dependence of Solvents, PH, Molar Ratio and Temperature in Tuning Metal Organic Framework Architecture. *Arabian Journal of Chemistry* **2019**, *12* (3), 295–315. https://doi.org/10.1016/j.arabjc.2016.01.003.

(43) Gao, Q.; Xie, Y.-B.; Li, J.-R.; Yuan, D.-Q.; Yakovenko, A. A.; Sun, J.-H.; Zhou, H.-C. Tuning the Formations of Metal–Organic Frameworks by Modification of Ratio of Reactant, Acidity of Reaction System, and Use of a Secondary Ligand. *Cryst Growth Des* **2012**, *12* (1), 281–288. https://doi.org/10.1021/cg201059d.

(44) Misran, H.; Adminuddin, A. M.; Zini, F. A. M.; Singh, R. Synthesis and Structural Consideration of Metal-Organic Framework (MOF) Coordination Polymer with Various Metal Linker Ratios. *Key Eng Mater* **2011**, *462–463* (3), 1103–1108. https://doi.org/10.4028/www.scientific.net/KEM.462-463.1103.

(45) Liu, Y.; Liu, S.; Gonçalves, A. A. S.; Jaroniec, M. Effect of Metal-Ligand Ratio on the CO2 Adsorption Properties of Cu-BTC Metal-Organic Frameworks. *RSC Adv* **2018**, *8* (62), 35551–35556. https://doi.org/10.1039/c8ra07774f.

(46) Laybourn, A.; Katrib, J.; Ferrari-John, R. S.; Morris, C. G.; Yang, S.; Udoudo, O.; Easun, T. L.; Dodds, C.; Champness, N. R.; Kingman, S. W.; Schröder, M. Metal–

Organic Frameworks in Seconds via Selective Microwave Heating. *J Mater Chem A Mater* **2017**, *5* (16), 7333–7338. https://doi.org/10.1039/C7TA01493G.

(47) Bazer-Bachi, D.; Assié, L.; Lecocq, V.; Harbuzaru, B.; Falk, V. Towards Industrial Use of Metal-Organic Framework: Impact of Shaping on the MOF Properties. *Powder Technol* **2014**, *255*, 52–59. https://doi.org/https://doi.org/10.1016/j.powtec.2013.09.013.

(48) Ursueguía, D.; Díaz, E.; Ordóñez, S. Densification-Induced Structure Changes in Basolite MOFs: Effect on Low-Pressure CH4 Adsorption. *Nanomaterials* **2020**, *10* (6), 1089. https://doi.org/10.3390/nano10061089.

(49) Guo, H.; Zhu, Y.; Wang, S.; Su, S.; Zhou, L.; Zhang, H. Combining Coordination Modulation with Acid–Base Adjustment for the Control over Size of Metal–Organic Frameworks. *Chemistry of Materials* **2012**, *24* (3), 444–450. https://doi.org/10.1021/cm202593h.

(50) Luo, L.; Lv, G.-C.; Wang, P.; Liu, Q.; Chen, K.; Sun, W.-Y. PH-Dependent Cobalt(Ii) Frameworks with Mixed 3,3′,5,5′-Tetra(1H-Imidazol-1-Yl)-1,1′-Biphenyl and 1,3,5-Benzenetricarboxylate Ligands: Synthesis, Structure and Sorption Property. *CrystEngComm* **2013**, *15* (45), 9537–9543. https://doi.org/10.1039/C3CE41056K.

(51) Nouar, F.; Devic, T.; Chevreau, H.; Guillou, N.; Gibson, E.; Clet, G.; Daturi, M.; Vimont, A.; Marc Grenèche, J.; Breeze, M. I.; Walton, R. I.; Llewellyn, P. L.; Serre, C. Tuning the Breathing Behaviour of MIL-53 by Cation Mixing. *Chemical Communications* **2012**, *48* (82), 10237–10239. https://doi.org/10.1039/c2cc35348b.

(52) Abednatanzi, S.; Gohari Derakhshandeh, P.; Depauw, H.; Coudert, F. X.; Vrielinck, H.; Van Der Voort, P.; Leus, K. Mixed-Metal Metal-Organic Frameworks. *Chem Soc Rev* **2019**, *48* (9), 2535–2565. https://doi.org/10.1039/c8cs00337h.

(53) Zhai, Q.-G.; Bu, X.; Mao, C.; Zhao, X.; Feng, P. Systematic and Dramatic Tuning on Gas Sorption Performance in Heterometallic Metal–Organic Frameworks. *J Am Chem Soc* **2016**, *138* (8), 2524–2527. https://doi.org/10.1021/jacs.5b13491.

(54) Gaikwad, R.; Gaikwad, S.; Han, S. Bimetallic UTSA-16 (Zn, X; X = Mg, Mn, Cu) Metal Organic Framework Developed by a Microwave Method with Improved CO2capture Performances. *Journal of Industrial and Engineering Chemistry* **2022**, *111*, 346–355. https://doi.org/10.1016/j.jiec.2022.04.016.

(55) Newbury, D. E.; Ritchie, N. W. M. Is Scanning Electron Microscopy/Energy Dispersive X-Ray Spectrometry (SEM/EDS) Quantitative? *Scanning* **2013**, *35* (3), 141–168. https://doi.org/10.1002/sca.21041.

(56) Wang, L. J.; Deng, H.; Furukawa, H.; Gándara, F.; Cordova, K. E.; Peri, D.; Yaghi, O. M. Synthesis and Characterization of Metal–Organic Framework-74 Containing 2, 4, 6, 8, and 10 Different Metals. *Inorg Chem* **2014**, *53* (12), 5881–5883. https://doi.org/10.1021/ic500434a.

(57) Abdoli, Y.; Razavian, M.; Fatemi, S. Bimetallic Ni–Co-Based Metal–Organic Framework: An Open Metal Site Adsorbent for Enhancing CO2 Capture. *Appl Organomet Chem* **2019**, *33* (8), 1–14. https://doi.org/10.1002/aoc.5004.

(58) Hon Lau, C.; Babarao, R.; Hill, M. R. A Route to Drastic Increase of CO2 Uptake in Zr Metal Organic Framework UiO-66. *Chemical Communications* **2013**, *49* (35), 3634–3636. https://doi.org/10.1039/C3CC40470F.

(59) Ahrens, L. H. The Use of Ionization Potentials Part 1. Ionic Radii of the Elements. *Geochim Cosmochim Acta* **1952**, *2* (3), 155–169. https://doi.org/https://doi.org/10.1016/0016-7037(52)90004-5.

(60) Zhou, Z.; Mei, L.; Ma, C.; Xu, F.; Xiao, J.; Xia, Q.; Li, Z. A Novel Bimetallic MIL-101(Cr, Mg) with High CO2 Adsorption Capacity and CO2/N2 Selectivity. *Chem Eng Sci* **2016**, *147*, 109–117. https://doi.org/10.1016/j.ces.2016.03.035.

(61) Masala, A.; Vitillo, J. G.; Bonino, F.; Manzoli, M.; Grande, C. A.; Bordiga, S. New Insights into UTSA-16. *Physical Chemistry Chemical Physics* **2016**, *18* (1), 220–227. https://doi.org/10.1039/C5CP05905D.

(62) Masala, A.; Grifasi, F.; Atzori, C.; Vitillo, J. G.; Mino, L.; Bonino, F.; Chierotti, M. R.; Bordiga, S. CO 2 Adsorption Sites in UTSA-16: Multitechnique Approach. *The Journal of Physical Chemistry C* **2016**, *120* (22), 12068–12074. https://doi.org/10.1021/acs.jpcc.6b03333.

(63) Forgan, R. S. Modulated Self-Assembly of Metal–Organic Frameworks. *Chem Sci* **2020**, *11* (18), 4546–4562. https://doi.org/10.1039/D0SC01356K.

(64) Yang, L.; Zhao, T.; Boldog, I.; Janiak, C.; Yang, X.-Y.; Li, Q.; Zhou, Y.-J.; Xia, Y.; Lai, D.-W.; Liu, Y.-J. Benzoic Acid as a Selector–Modulator in the Synthesis of MIL-88B(Cr) and Nano-MIL-101(Cr). *Dalton Transactions* **2019**, *48* (3), 989–996. https://doi.org/10.1039/C8DT04186E.

(65) Banerjee, D.; Finkelstein, J.; Smirnov, A.; Forster, P. M.; Borkowski, L. A.; Teat, S. J.; Parise, J. B. Synthesis and Structural Characterization of Magnesium Based Coordination Networks in Different Solvents. *Cryst Growth Des* **2011**, *11* (6), 2572–2579. https://doi.org/10.1021/cg200327y.

(66) Mazaj, M.; Birsa Čelič, T.; Mali, G.; Rangus, M.; Kaučič, V.; Zabukovec Logar, N. Control of the Crystallization Process and Structure Dimensionality of Mg-Benzene-1,3,5-Tricarboxylates by Tuning Solvent Composition. *Cryst Growth Des* **2013**, *13* (8), 3825–3834. https://doi.org/10.1021/cg400929z.

(67) Schwolow, S.; Hollmann, J.; Schenkel, B.; Röder, T. Application-Oriented Analysis of Mixing Performance in Microreactors. *Org Process Res Dev* **2012**, *16* (9), 1513–1522. https://doi.org/10.1021/op300107z.

(68) Hone, C. A.; Kappe, C. O. Towards the Standardization of Flow Chemistry Protocols for Organic Reactions. *Chemistry–Methods* **2021**, *1* (11), 454–467. https://doi.org/10.1002/cmtd.202100059.

(69) Noel, T.; Capaldo, L.; Wen, Z. A Field Guide to Flow Chemistry for Synthetic Organic Chemists. *Chem Sci* **2023**, 4230–4247. https://doi.org/10.1039/d3sc00992k.

(70) Reckamp, J. M.; Bindels, A.; Duffield, S.; Liu, Y. C.; Bradford, E.; Ricci, E.; Susanne, F.; Rutter, A. Mixing Performance Evaluation for Commercially Available Micromixers Using Villermaux-Dushman Reaction Scheme with the Interaction by Exchange with the Mean Model. *Org Process Res Dev* **2017**, *21* (6), 816–820. https://doi.org/10.1021/acs.oprd.6b00332.

(71) Mulyati, T.; Ediati, R.; Rosyidah, A. Influence of Solvothermal Temperatures and Times on Crystallinity and Morphology of MOF-5. *Indonesian Journal of Chemistry* **2015**, *15*, 101–107. https://doi.org/10.22146/ijc.21202.

(72) Cheetham, A. K.; Kieslich, G.; Yeung, H. H.-M. Thermodynamic and Kinetic Effects in the Crystallization of Metal–Organic Frameworks. *Acc Chem Res* **2018**, *51* (3), 659–667. https://doi.org/10.1021/acs.accounts.7b00497.

(73) Zhang, K.-L.; Hou, C.-T.; Song, J.-J.; Deng, Y.; Li, L.; Ng, S. W.; Diao, G.-W. Temperature and Auxiliary Ligand-Controlled Supramolecular Assembly in a Series of Zn(Ii)-Organic Frameworks: Syntheses, Structures and Properties. *CrystEngComm* **2012**, *14* (2), 590–600. https://doi.org/10.1039/C1CE05577A.

(74) Cui, P.; Ren, L.; Chen, Z.; Hu, H.; Zhao, B.; Shi, W.; Cheng, P. Temperature-Controlled Chiral and Achiral Copper Tetrazolate Metal–Organic Frameworks: Syntheses, Structures, and I2 Adsorption. *Inorg Chem* **2012**, *51* (4), 2303–2310. https://doi.org/10.1021/ic2023105.

(75) Fonseca, J.; Gong, T.; Jiao, L.; Jiang, H.-L. Metal–Organic Frameworks (MOFs) beyond Crystallinity: Amorphous MOFs, MOF Liquids and MOF Glasses. *J Mater Chem A Mater* **2021**, *9* (17), 10562–10611. https://doi.org/10.1039/D1TA01043C.

(76) Hara, Y.; Kanamori, K.; Nakanishi, K. Self-Assembly of Metal–Organic Frameworks into Monolithic Materials with Highly Controlled Trimodal Pore Structures. *Angewandte Chemie International Edition* **2019**, *58* (52), 19047–19053. https://doi.org/https://doi.org/10.1002/anie.201911499.

(77) Elfving, J.; Kauppinen, J.; Jegoroff, M.; Ruuskanen, V.; Järvinen, L.; Sainio, T. Experimental Comparison of Regeneration Methods for CO2 Concentration from Air Using Amine-Based Adsorbent. *Chemical Engineering Journal* **2021**, *404*, 126337. https://doi.org/https://doi.org/10.1016/j.cej.2020.126337.

(78) Gunawan, T.; Wijiyanti, R.; Widiastuti, N. Adsorption–Desorption of CO2 on Zeolite-Y-Templated Carbon at Various Temperatures. *RSC Adv* **2018**, *8* (72), 41594–41602. https://doi.org/10.1039/C8RA09200A.

(79) Rubio-Martinez, M.; Avci-Camur, C.; Thornton, A. W.; Imaz, I.; Maspoch, D.; Hill, M. R. New Synthetic Routes towards MOF Production at Scale. *Chem Soc Rev* **2017**, *46* (11), 3453–3480. https://doi.org/10.1039/C7CS00109F.

(80) Addicoat, M.; Au, V. K.-M.; Brammer, L.; Burrows, A.; Casaban, J.; D'Alessandro, D. M.; Fucci, R.; Horcajada, P.; Humphrey, S.; Kitagawa, S.; Lavenn, C.; Laybourn, A.; Li, H.; Li, J.; Li, Q.; Li, Y.; Mukherjee, S.; Otake, K.; Patel, K.; Pinto, M.; Schroder,

M.; Serre, C.; Szilágyi, P.; Thomas, O.; Yang, S.; Zhou, G. Commercialisation and Applications: General Discussion. *Faraday Discuss* **2021**, *231* (0), 384–396. https://doi.org/10.1039/D1FD90059E.

(81) Rasmussen, E. G.; Kramlich, J.; Novosselov, I. V. Scalable Continuous Flow Metal–Organic Framework (MOF) Synthesis Using Supercritical CO2. *ACS Sustain Chem Eng* **2020**, *8* (26), 9680–9689. https://doi.org/10.1021/acssuschemeng.0c01429.

(82) Howarth, A. J.; Peters, A. W.; Vermeulen, N. A.; Wang, T. C.; Hupp, J. T.; Farha, O. K. Best Practices for the Synthesis, Activation, and Characterization of Metal–Organic Frameworks. *Chemistry of Materials* **2017**, *29* (1), 26–39. https://doi.org/10.1021/acs.chemmater.6b02626.

(83) Li, H.; Sadiq, M. M.; Suzuki, K.; Ricco, R.; Doblin, C.; Hill, A. J.; Lim, S.; Falcaro, P.; Hill, M. R. Magnetic Metal–Organic Frameworks for Efficient Carbon Dioxide Capture and Remote Trigger Release. *Advanced Materials* **2016**, *28* (9), 1839–1844. https://doi.org/10.1002/adma.201505320.

(84) He, B.; Sadiq, M. M.; Batten, M. P.; Suzuki, K.; Rubio-Martinez, M.; Gardiner, J.; Hill, M. R. Continuous Flow Synthesis of a Zr Magnetic Framework Composite for Post-Combustion CO 2 Capture. *Chemistry – A European Journal* **2019**, *25* (57), 13184–13188. https://doi.org/10.1002/chem.201902560.

(85) Li, H.; Sadiq, M. M.; Suzuki, K.; Ricco, R.; Doblin, C.; Hill, A. J.; Lim, S.; Falcaro, P.; Hill, M. R. Magnetic Metal–Organic Frameworks for Efficient Carbon Dioxide Capture and Remote Trigger Release. *Advanced Materials* **2016**, *28* (9), 1839–1844. https://doi.org/10.1002/adma.201505320.

(86) Li, H.; Sadiq, M. M.; Suzuki, K.; Doblin, C.; Lim, S.; Falcaro, P.; Hill, A. J.; Hill, M. R. MaLISA – a Cooperative Method to Release Adsorbed Gases from Metal–Organic

Frameworks. *J Mater Chem A Mater* **2016**, *4* (48), 18757–18762. https://doi.org/10.1039/C6TA09826F.

(87) Railey, P.; Song, Y.; Liu, T.; Li, Y. Metal Organic Frameworks with Immobilized Nanoparticles: Synthesis and Applications in Photocatalytic Hydrogen Generation and Energy Storage. *Mater Res Bull* **2017**, *96*, 385–394. https://doi.org/https://doi.org/10.1016/j.materresbull.2017.04.020.

(88) Yang, Q.; Xu, Q.; Jiang, H.-L. Metal–Organic Frameworks Meet Metal Nanoparticles: Synergistic Effect for Enhanced Catalysis. *Chem Soc Rev* **2017**, *46* (15), 4774–4808. https://doi.org/10.1039/C6CS00724D.

(89) Abdi, J.; Hadavimoghaddam, F.; Hadipoor, M.; Hemmati-Sarapardeh, A. Modeling of CO2 Adsorption Capacity by Porous Metal Organic Frameworks Using Advanced Decision Tree-Based Models. *Sci Rep* **2021**, *11* (1), 1–14. https://doi.org/10.1038/s41598-021-04168-w.

(90) Ding, M.; Cai, X.; Jiang, H.-L. Improving MOF Stability: Approaches and Applications. *Chem Sci* **2019**, *10* (44), 10209–10230. https://doi.org/10.1039/C9SC03916C.

(91) Li, Z.; Liu, P.; Ou, C.; Dong, X. Porous Metal–Organic Frameworks for Carbon Dioxide Adsorption and Separation at Low Pressure. *ACS Sustain Chem Eng* **2020**, *8* (41), 15378–15404. https://doi.org/10.1021/acssuschemeng.0c05155.

(92) Molinar-Díaz, J.; Woodliffe, J. L.; Steer, E.; Morley, N. A.; Brown, P. D.; Ahmed, I. Optimisation of the Flame Spheroidisation Process for the Rapid Manufacture of Fe3O4-Based Porous and Dense Microspheres. *Molecules* **2023**, *28* (6), 2523. https://doi.org/10.3390/molecules28062523.

(93) Li, J.; Gao, H.; Tan, L.; Luan, Y.; Yang, M. Superparamagnetic Core–Shell Metal–Organic Framework Fe3O4/Cu3(Btc)2 Microspheres and Their Catalytic Activity in the Aerobic Oxidation of Alcohols and Olefins. *Eur J Inorg Chem* **2016**, *2016* (30), 4906–4912. https://doi.org/10.1002/ejic.201600761.

(94) Ke, F.; Qiu, L.-G.; Yuan, Y.-P.; Jiang, X.; Zhu, J.-F. Fe3O4@MOF Core–Shell Magnetic Microspheres with a Designable Metal–Organic Framework Shell. *J Mater Chem* **2012**, *22* (19), 9497–9500. https://doi.org/10.1039/C2JM31167D.

(95) Zhang, T.; Zhang, X.; Yan, X.; Kong, L.; Zhang, G.; Liu, H.; Qiu, J.; Yeung, K. L. Synthesis of Fe3O4@ZIF-8 Magnetic Core–Shell Microspheres and Their Potential Application in a Capillary Microreactor. *Chemical Engineering Journal* **2013**, *228*, 398–404. https://doi.org/https://doi.org/10.1016/j.cej.2013.05.020.

(96) Melag, L.; Sadiq, M. M.; Smith, S. J. D.; Konstas, K.; Suzuki, K.; Hill, M. R. Efficient Delivery of Oxygen via Magnetic Framework Composites. *J Mater Chem A Mater* **2019**, *7* (8), 3790–3796. https://doi.org/10.1039/C8TA07739H.

(97) Chen, S. J.; Zhu, M.; Fu, Y.; Huang, Y. X.; Tao, Z. C.; Li, W. L. Using 13X, LiX, and LiPdAgX Zeolites for CO2 Capture from Post-Combustion Flue Gas. *Appl Energy* **2017**, *191*, 87–98. https://doi.org/https://doi.org/10.1016/j.apenergy.2017.01.031.

(98) Creamer, A. E.; Gao, B. Carbon-Based Adsorbents for Postcombustion CO 2 Capture: A Critical Review. *Environ Sci Technol* **2016**, *50* (14), 7276–7289. https://doi.org/10.1021/acs.est.6b00627.

(99) Yassin, M. M.; Anderson, J. A.; Dimitrakis, G. A.; Martín, C. F. Effects of the Heating Source on the Regeneration Performance of Different Adsorbents under Post-Combustion Carbon Capture Cyclic Operations. A Comparative Analysis. *Sep Purif Technol* **2021**, *276*, 119326. https://doi.org/10.1016/j.seppur.2021.119326.

(100) Morales-Ospino, R.; Santiago, R. G.; Siqueira, R. M.; de Azevedo, D. C. S.; Bastos-Neto, M. Assessment of CO2 Desorption from 13X Zeolite for a Prospective TSA Process. *Adsorption* **2020**, *26* (5), 813–824. https://doi.org/10.1007/s10450-019-00192-5.

(101) Sadiq, M. M.; Rubio-Martinez, M.; Zadehahmadi, F.; Suzuki, K.; Hill, M. R. Magnetic Framework Composites for Low Concentration Methane Capture. *Ind Eng Chem Res* **2018**, *57* (18), 6040–6047. https://doi.org/10.1021/acs.iecr.8b00810.